Refraction analysis of the Blackfoot 2D-3C data

Jocelyn Dufour, and Don C. Lawton

ABSTRACT

A three-component 2D seismic line was acquired in the Blackfoot Field area in 1995 by the CREWES project. The area is covered of glacial deposits and shale. These low velocity near-surface deposits induce time delays for the recording of *P*-wave and *S*-wave reflection seismic data. Refraction analysis can help resolve these delays by determining near-surface models. *S*-wave refractions were identified on the radial component of the Blackfoot 2D-3C dataset and were used to establish a *S*-wave near-surface model, while *P*-wave refraction were used to build the *P*-wave model. Two refraction method were used: the Plus-Minus time analysis method and the Generalized Linear Inversion method. The subweathering thickness for both *P* and *S*-wave near-surface model was established at 94 meters. The average *P*-wave velocity for this layer is 1968 m/s and around 3100 m/s for the second layer, while the average *S*-wave velocity is 465 m/s for the first layer and around 1200 m/s for the second layer. The V_P/V_S ratio of the first layer is 4.2 and 2.5 for the second layer. According to the *P*-*S* reflection raypath geometry, the shot static corrections were computed from the *P*-wave model and the receiver static correction from the *S*-wave model and were applied to the radial component data. Some improvements were noticed in term of intermediate wavelength reflector structure and reflector continuity. However, the improvement is not as clear as with the application of the static corrections on the vertical component. The results of the Plus-Minus time analysis and Generalized Linear Inversion methods are consistent in term of depths, velocities, static corrections. However, the Plus-Minus time analysis method provides a more detailed model than Generalized Linear Inversion method.

INTRODUCTION

In the Blackfoot Field area, 15 km east south east of Strathmore (Alberta), a three-component 2D seismic survey was acquired in 1995 by the CREWES project. The presence of an irregular thickness of poorly compacted near-surface deposits induces time delays for the recording of *P*-wave and *S*-wave reflection seismic data. The near-surface deposits in the region of Blackfoot are composed of a thin surficial layer of glacial deposits (less than 10 meter) and a low velocity sedimentary layer (figure 1). The glacial deposits are mainly moraine (till) and lake (clay) deposits (Stalker, 1957). The area was glaciated by both Laurentide and Cordilleran ice during Pleistocene and till was deposited. The glaciolacustrine (lake) deposits were deposited beyond the glaciers, and during the nonglacial interval that followed the Pleistocene glacial interval (Teller and Clayton, 1983). In the northwest of the region, the first sedimentary layer, which corresponds to the bedrock in figure 1, is a shale interbedded with fine-grained sandstone and coal (Paskapoo Formation, Tertiary), while in the east and south of the region, the sedimentary layer is an argillaceous sandstone (Edmonton Formation, Cretaceous) with some bentonitic shale (Irish, 1967). The seismic line crosses the two main type of glacial deposits (moraine and glaciolacustrine deposits) and lies over the Paskapoo Formation (figure 1). Water wells in the proximity of the seismic line indicates that the low velocity shale of the Paskapoo Formation goes to at least 70 meters below the surface.

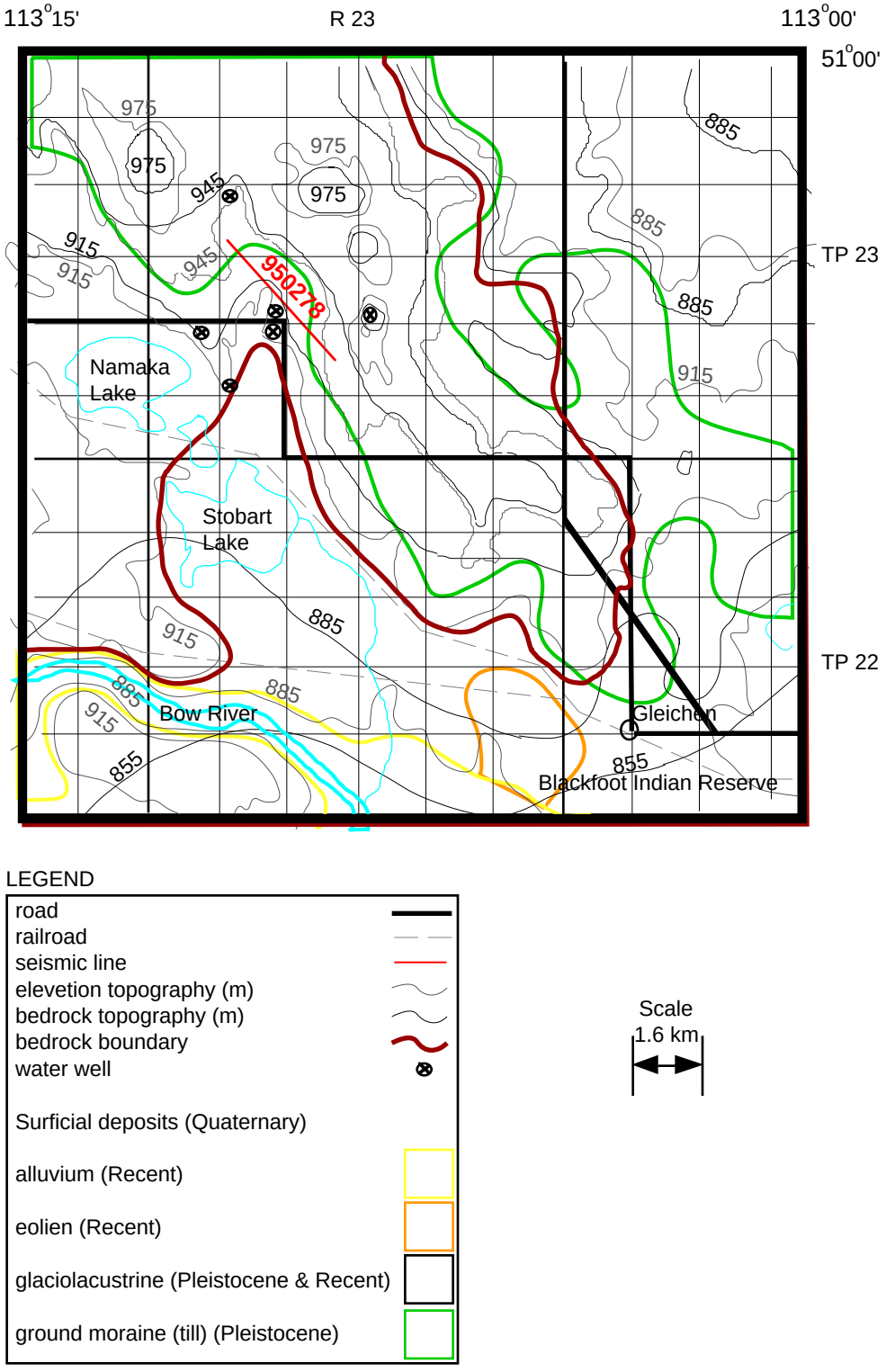

Figure 1. Near-surface geology map of the Blackfoot area modified from Stalker (1957), Geiger (1967) and Irish (1967).

Surface and near-surface effects can severely deteriorate the quality of reflection data, especially for the *S*-wave (Edelman and Helbig, 1983). The time delays affecting the *P*-*S* seismic data can be visualized by looking at the *P*-*S* reflection raypath

geometry. Figure 2 illustrates how *S*-wave reflection is recorded after a conversion from a *P*-wave energy.

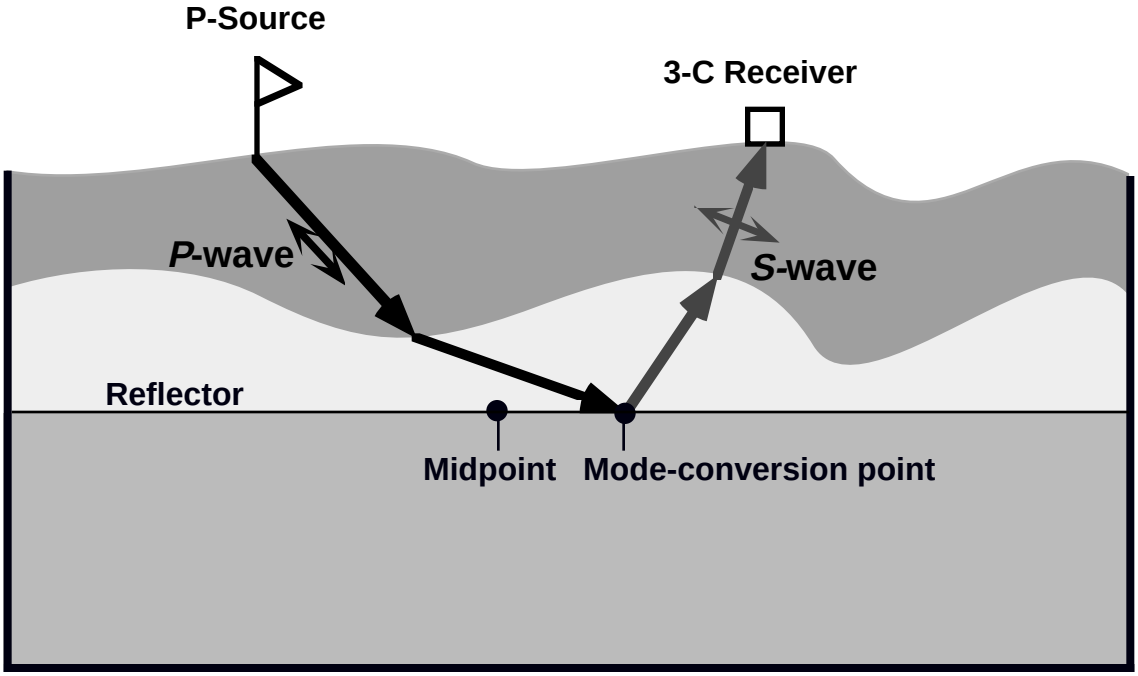

Figure 2. *P-S* reflection raypath geometry.

According to the *P-S* reflection raypath in figure 2, the downgoing wave travels as a *P*-wave energy from the source through the surface deposits until the reflector, then some of the energy is converted to a *S*-wave energy and travels back up to the surface to be recorded by a 3-component geophone. The *S*-wave energy should be recorded mainly on the horizontal components (radial and transverse). The radial component is in the same direction of the survey line, whereas the transverse component is perpendicular to the survey line. When no azimuthal anisotropy is present, the *S*-wave energy should be recorded mainly along the radial component (Cary and Eaton, 1993). The *S*-wave arrivals at the geophones are being delayed by the surface deposits, as a *P*-wave below the shot and as a *S*-wave below the receiver. To remove the shot delay, a near-surface *P*-wave model needs to be established, while to remove the receiver delay, a near-surface *S*-wave model needs to be built. The *S*-wave statics can not be approximated by scaling the *P*-wave static values, because they are unrelated (Anno, 1986). As an example, the *P*-waves are affected by near-surface fluctuations in the water table while the *S*-waves are not. The Plus-Minus time analysis method developed by Dufour and Foltinek (1996) and the Generalized Linear Inversion method of Hampson and Russell (1984) are used to establish the near-surface models. Their results are then compared according to the accuracy of the model, the static corrections and their impact on the reflection data.

SHEAR-REFRACTION ANALYSIS

Identification of S-wave refracted arrivals

P-wave refraction analysis is well known and is used to establish a near-surface *P*-wave model, from which static corrections are computed. However, *S*-wave refracted arrivals are not generally used to establish a near-surface *S*-wave model and to compute static corrections that are associated with severe time delays affecting the *P-S* data.

This is primarily because *S*-wave refracted arrivals are often masked by *P*-wave data superimposed (leaking) onto the radial component. Instead of using the refracted arrivals, the static corrections are usually determined by a hand picking process using common receiver stacks, which can bias the picks (Cary and Eaton, 1993). Also, real reflector structure can be flattened. *S*-wave refraction events have been identified on the radial component data (in between dashed line in figure 3). These events are interpreted to be shear head-wave arrivals rather than Rayleigh wave events because their polarization is approximately rectilinear rather than elliptical (Jolly and Mifsud, 1971).

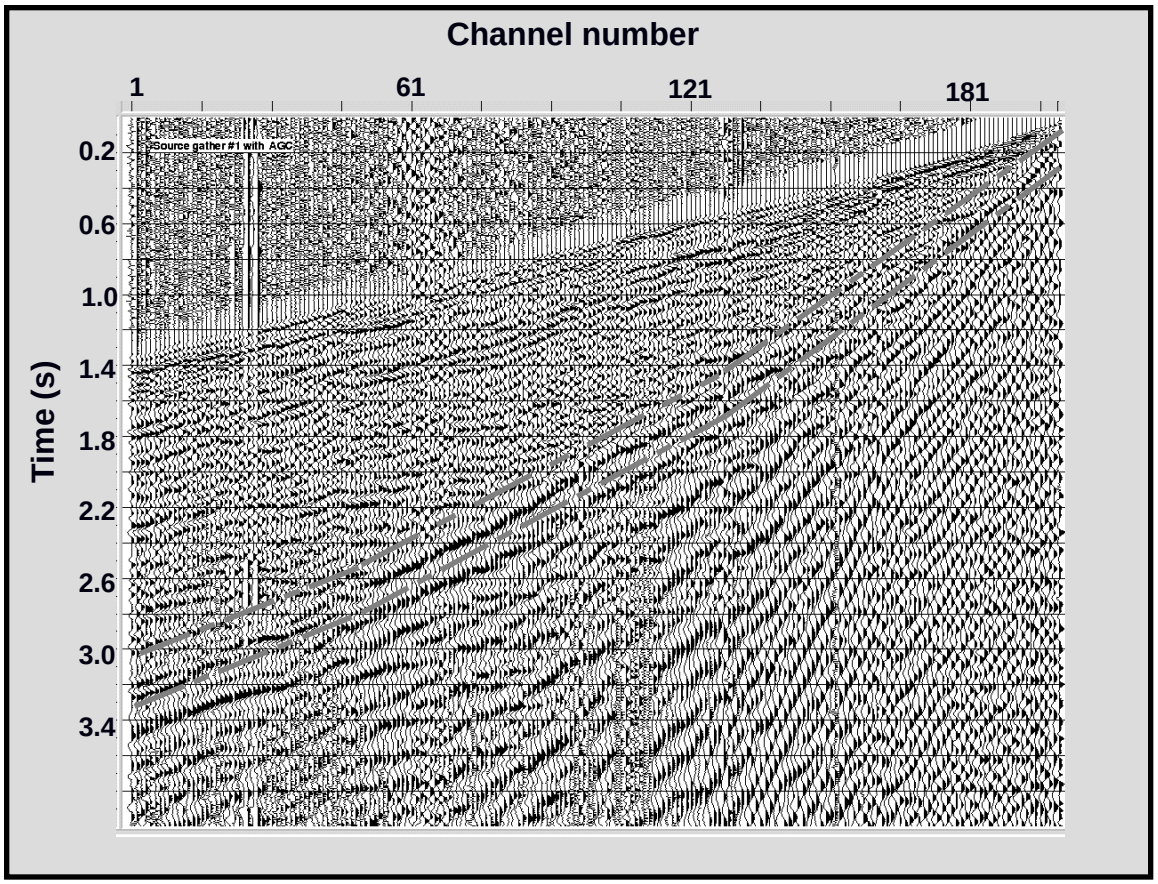

Figure 3. Radial component from the Blackfoot dataset (shot gather #1).

To help understand and determine the polarization of different events, three domains including the shear head-wave arrivals were picked on the vertical and radial components (figures 4 and 5, respectively). Figure 6 shows the relative amplitude of the shear head-wave arrivals (*S*-wave refractions) on the radial and vertical component data. It can be noticed that the amplitude is approximately linear in the radial component direction, which shows that the event is received mainly in the horizontal direction. *P*-wave refraction events also have a rectilinear polarization but in the vertical component direction (figure 7), while Rayleigh wave events have an elliptical polarization (figure 8). Figure 9 summarizes the raypath geometry of these three type of events. The conversion from a *P*-wave to *S*-wave is believed to occur soon after the source explosion, so that the *S*-wave head-wave arrivals can be considered as pure *S*-wave refractions.

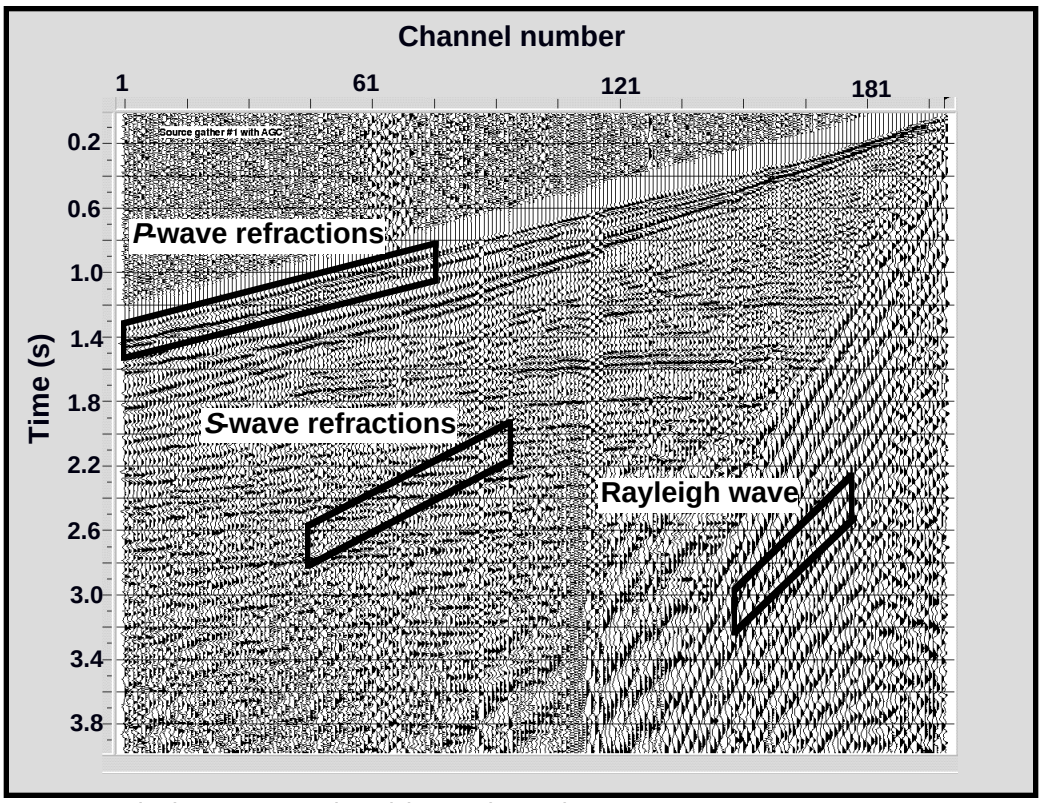

Figure 4. Vertical component data (shot gather #1).

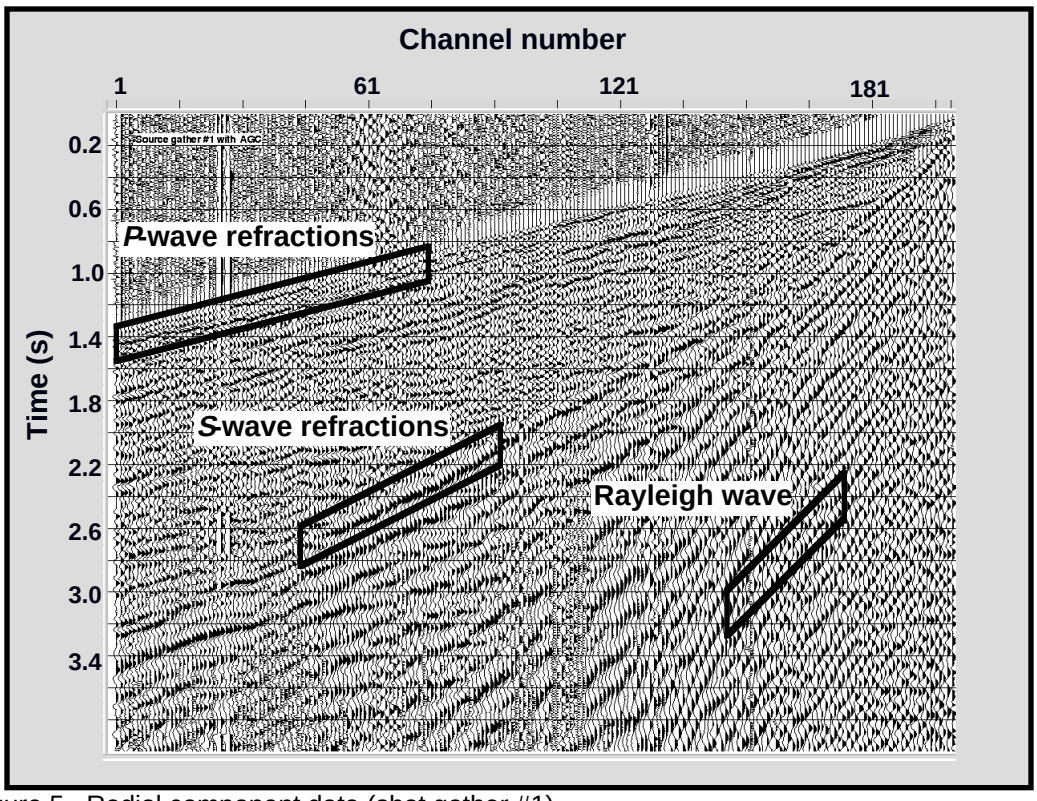

Figure 5. Radial component data (shot gather #1).

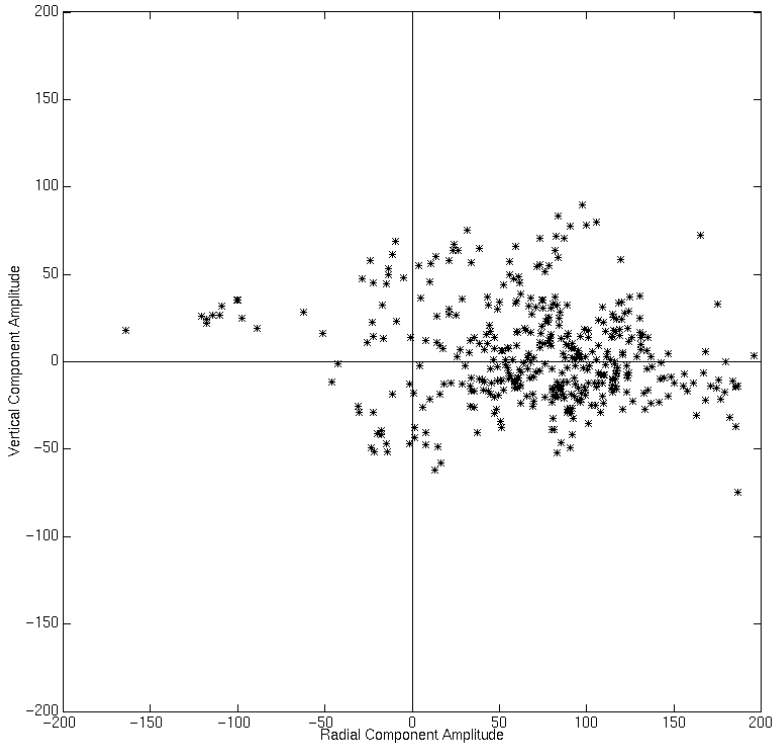

Figure 6. Relative vertical and radial component amplitude of the *S*-wave refractions.

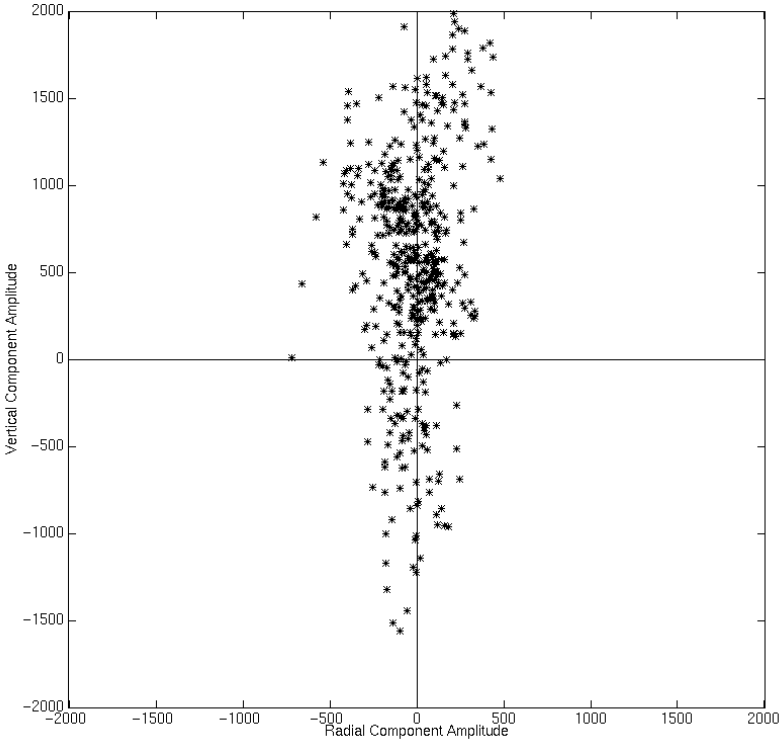

Figure 7. Relative vertical and radial component amplitude of the *P*-wave refractions.

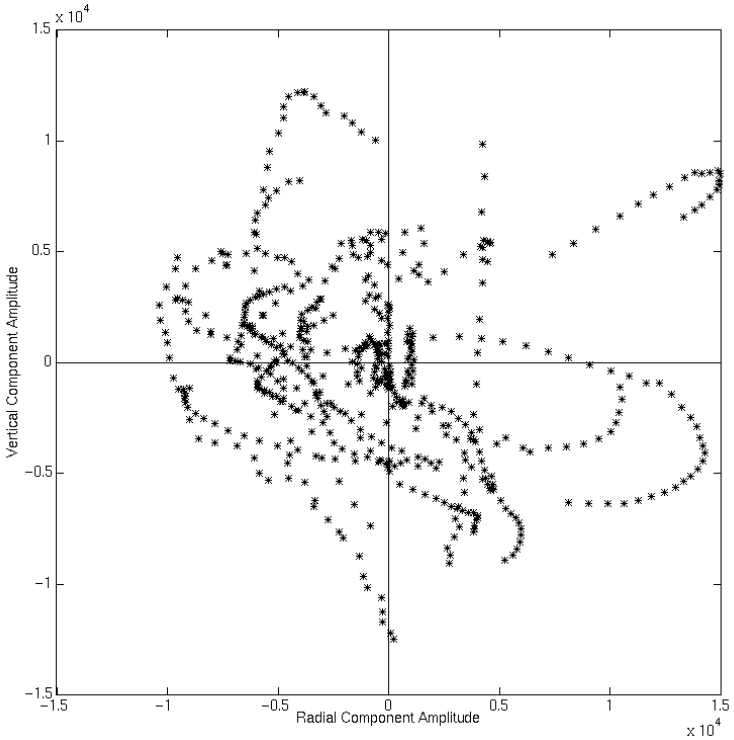

Figure 8. Relative vertical and radial component amplitude of the Rayleigh-wave.

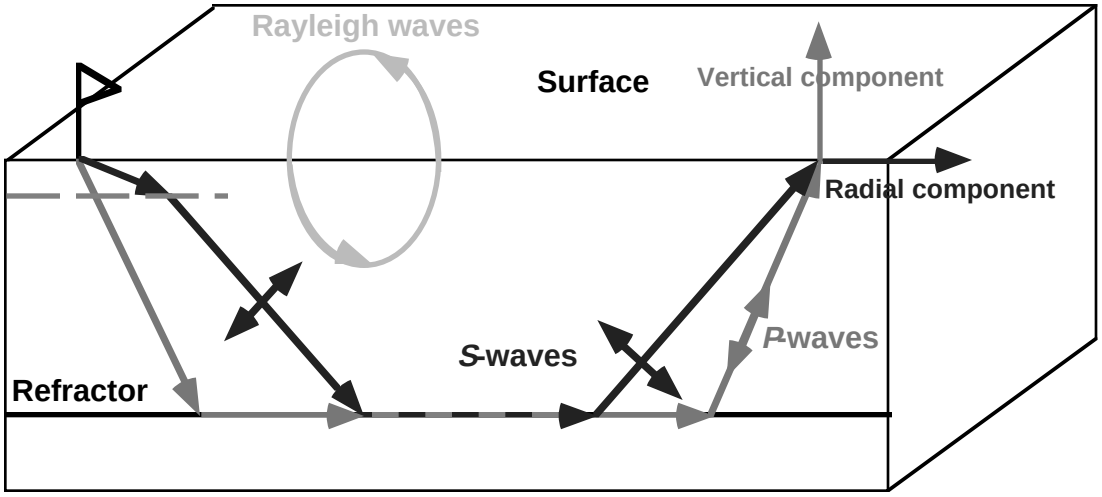

Figure 9. Raypath geometry of the Rayleigh-wave, the *S*-wave and *P*-wave refractions.

Signal enhancement

The main problem of using the *S*-wave refracted arrivals is that they are masked by the *P*-wave data and the *P*-*S* reflection data. In an effort to remove all signals and to keep only the *S*-wave refraction events, an *F*-*K* filter was applied to the radial component data. As a result of data filtering, the refracted arrivals were more easily and rapidly picked (figure 10). From these refracted arrival picks, any standard refraction static method can be used to establish a near-surface model and compute the receiver static corrections.

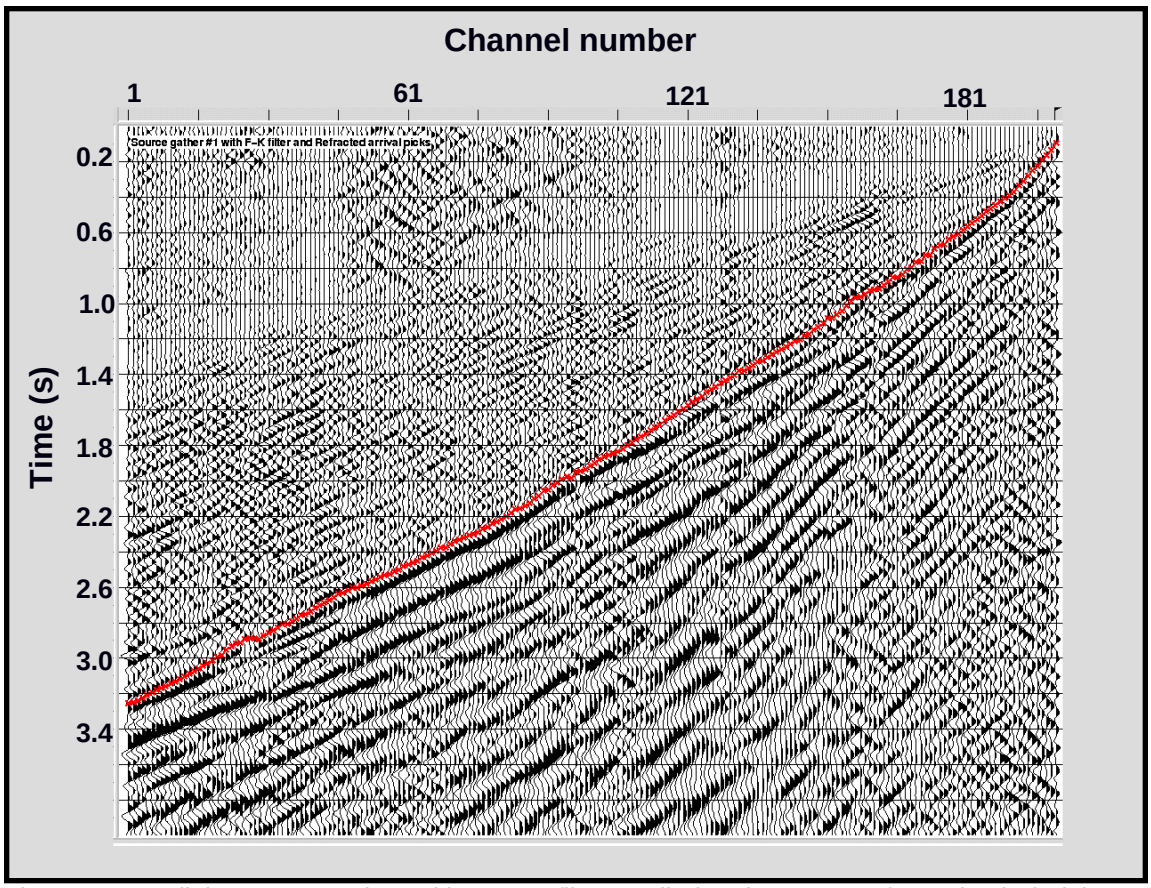

Figure 10. Radial component data with an F-K filter applied and S-wave refracted arrival picks (*) (shot gather # 1).

PLUS-MINUS TIME ANALYSIS METHOD

Two refraction static methods were used to find the *P* and *S* near-surface model. The first method used was the Plus-Minus time analysis method based on the plus-minus method of Hagedoorn (1959) (Dufour and Foltinek, 1996). The plus-minus method is an approximation of the wavefront reconstruction method by Thornburgh (1930). The plus-minus method includes two analysis: the Plus time analysis and the Minus time analysis. The Plus time analysis establish the depth to the refractor below the receivers, while the Minus time analysis finds the velocity of the refractor. The Generalized Linear Inversion by Hampson and Russell (1984) has been used to provide a comparison with the Plus-Minus time analysis method (next section).

Refracted arrivals

The *P*-wave refracted arrivals (first-breaks) were picked on the vertical component (figure 11), while the *S*-wave refracted arrivals were picked on the radial component (figure 12). It can be noticed that the *S*-wave refracted arrival traveltimes are more than twice the *P*-wave refracted arrival traveltimes. This is a consequence of slower velocity values for the *S*-wave than for the *P*-wave. Some of the *S*-wave refracted arrival traveltimes are absent due to difficulty in picking the event from the records.

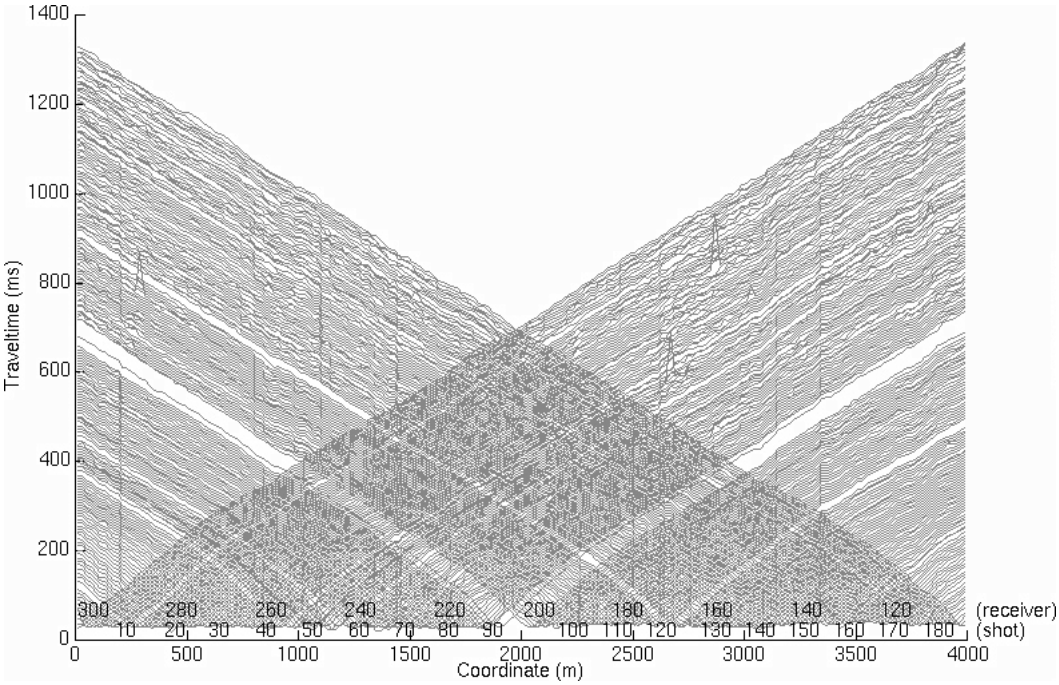

Figure 11. *P*-wave refracted arrival traveltimes from the vertical component.

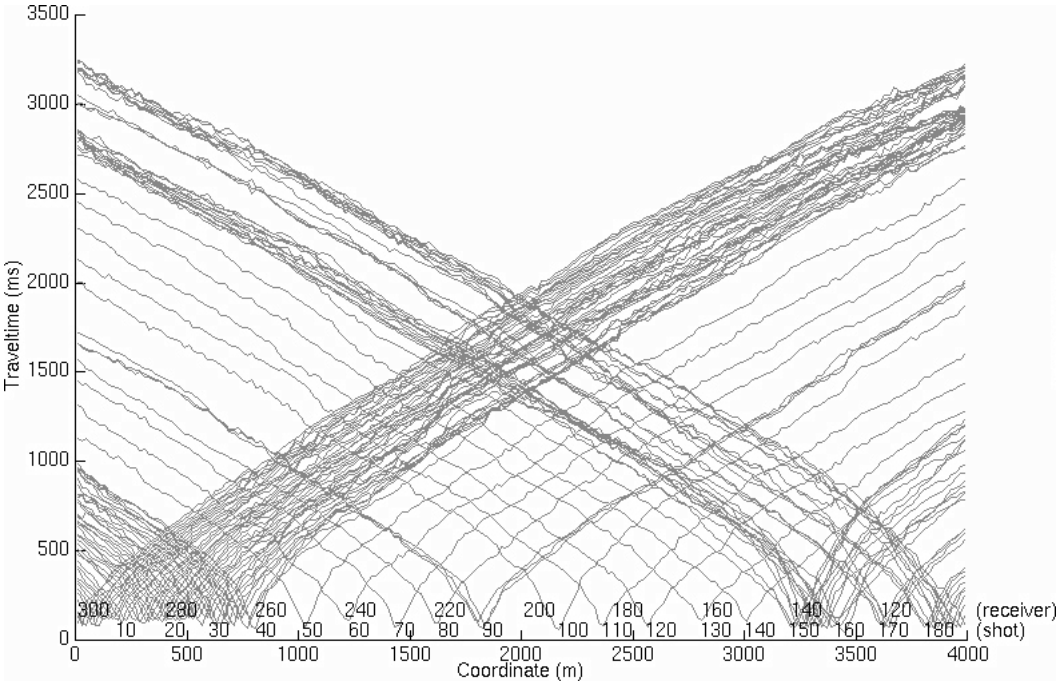

Figure 12. *S*-wave refracted arrival traveltimes from the radial component.

Reciprocal time differences

The plus-minus method of Hagedoorn (1959) is based on the traveltime reciprocity principle, which is that the traveltime of a seismic wave from a location to another location is the same in both direction (forward and reverse). The reciprocal time check process provides a bank of all the possible shot pair reciprocal traveltime differences. According to the reciprocity principle, the traveltime differences should be equal to zero. However, with real data and errors in arrival picking, nonzero traveltime differences are expected. The average reciprocal traveltime difference for the *P*-wave refractions is of 4 ms and of 47 ms for the *S*-wave refractions. This difference between the *P*-wave and *S*-wave refraction traveltime reciprocity is due to the fact that the *S*-wave refracted arrival traveltimes are at least twice the *P*-wave refracted arrival traveltimes and to larger picking error. A depth variation of the conversion from the source *P*-wave to *S*-wave along the survey line would also create more important reciprocal traveltime difference for the *S*-wave refracted arrivals. Therefore, the reciprocal traveltime differences were used to shift the traveltimes of one of the shot while using the Plus time analysis. The reciprocal traveltime difference will correct for raypath geometry complexity (inhomogeneities, thin layering, and depth conversion variation (*S*-wave refractions only)), picking errors and inaccuracy of the uphole times, which are being added to the arrival traveltimes.

Crossover points

The crossover point represents a change in the refracted arrivals from one layer to another. The identification of the crossover point locations will determine the Plus-Minus time analysis window limits. The crossover point autopicking process was undertaken on both refracted arrivals (*P* and *S*) using a median filter window length of 11 samples on the traveltime difference and a differentiation separation length of 3 samples for the first derivative (figures 13 and 14). The crossover point locations correspond to the maximum of the second derivative (Wang and Cheadle, 1995).

Once the crossover point autopicking processes using all the possible overlapping shot gathers were completed for both refracted arrivals (*P* and *S*), the crossover point averages were computed and some of them were edited to a proper location according to a consistent interpretation. Figure 15 shows the location of the crossover point averages on their respective arrival shot spreads for the *P*-wave refractions, while figure 16 displays the crossover point average offsets (from the corresponding shot location), the standard deviations and the fold. It can be noticed that the crossover point average offsets varies from 124 meters to 475 meters and that they generally increase at both ends of the survey, while the standard deviation goes from zero meter to 182 meters (average of 72 meters). The fold for the right crossover point averages decreases on the left extremity of the survey due to fewer overlapping shot spreads available, while the fold of the left crossover point average decreases on the right extremity of the survey. The maximum fold is 173 and the average is 87.

The equivalent displays are available for the *S*-wave refractions, so the location of the crossover point averages and their respective arrival shot spreads are shown in figure 17, while the crossover point average offsets, the standard deviations and the fold are illustrated by figure 18. The crossover point average offsets range from 70 meters to 286 meters, while the standard deviation goes from zero meter to 224 meters (average of 53 meters). The maximum fold is 69 and the average is 34.

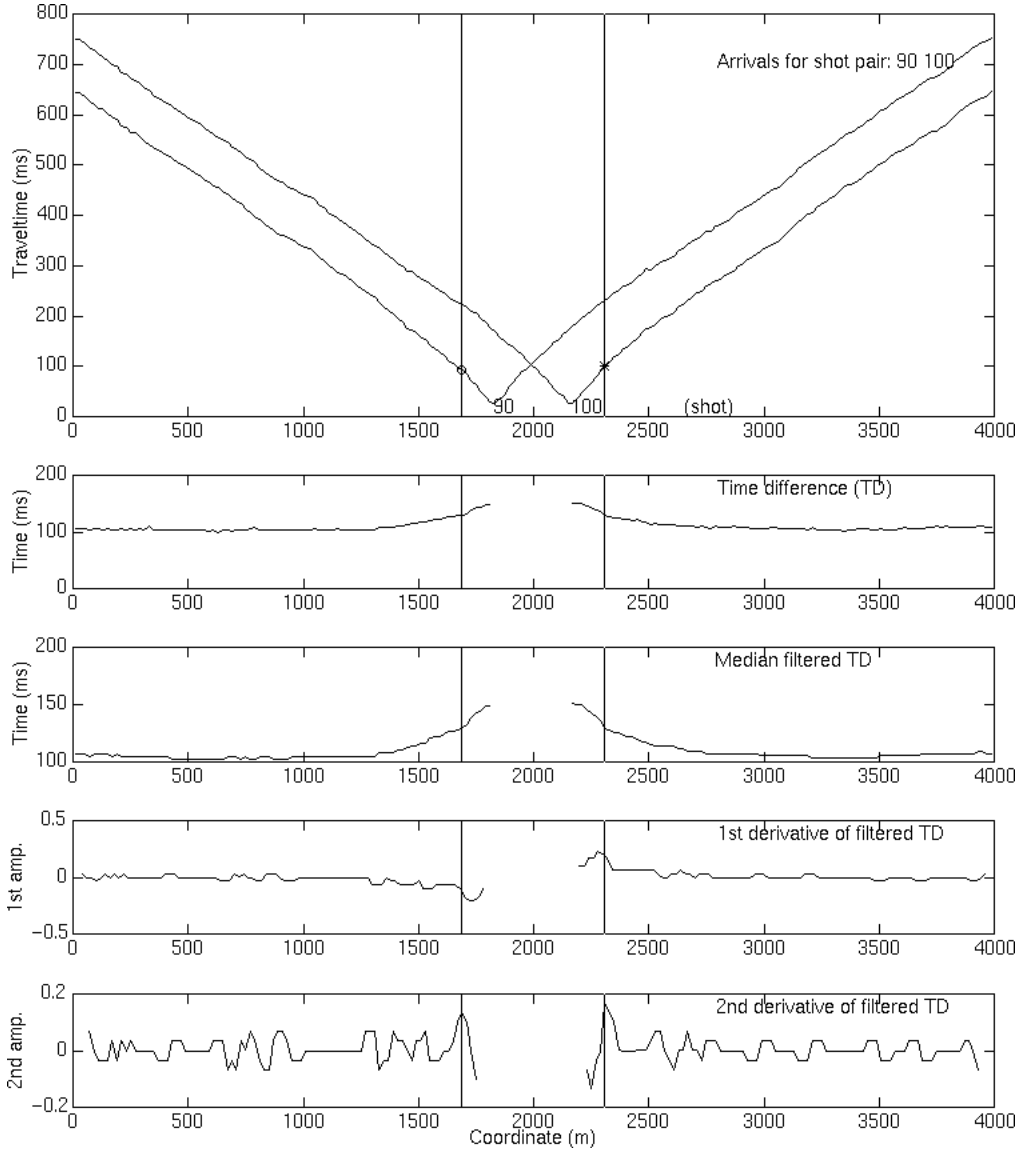

Figure 13. Crossover autopicking process for the left crossover point of shot gather #90 (o) and for the right crossover point of shot gather #100 (*) on the *P*-wave refractions (median filter window length of 11 samples and differentiation separation length of 3 samples).

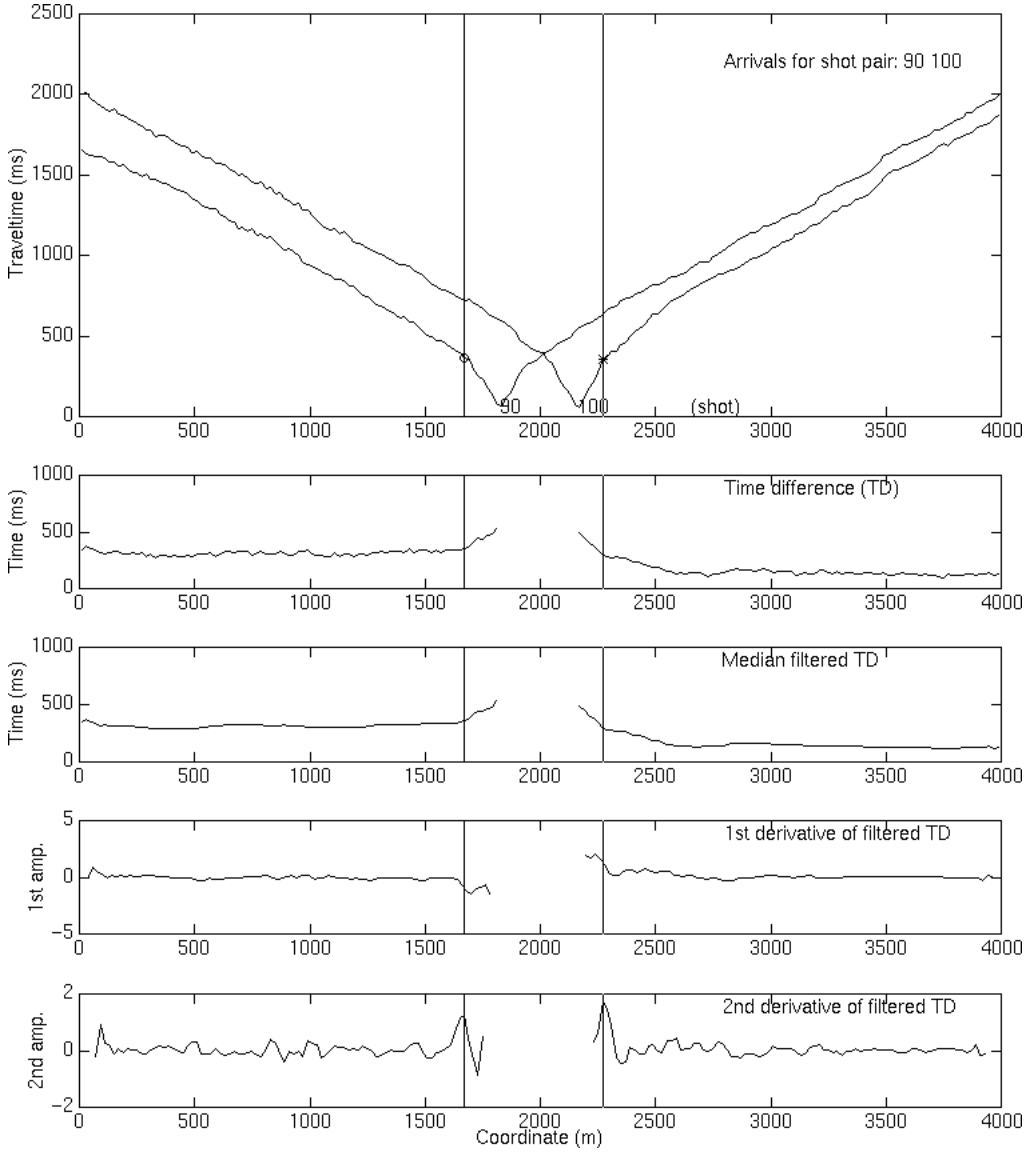

Figure 14. Crossover autopicking process for the left crossover point of shot gather #90 (o) and for the right crossover point of shot gather #100 (*) on the *S*-wave refractions (median filter window length of 11 samples and differentiation separation length of 3 samples).

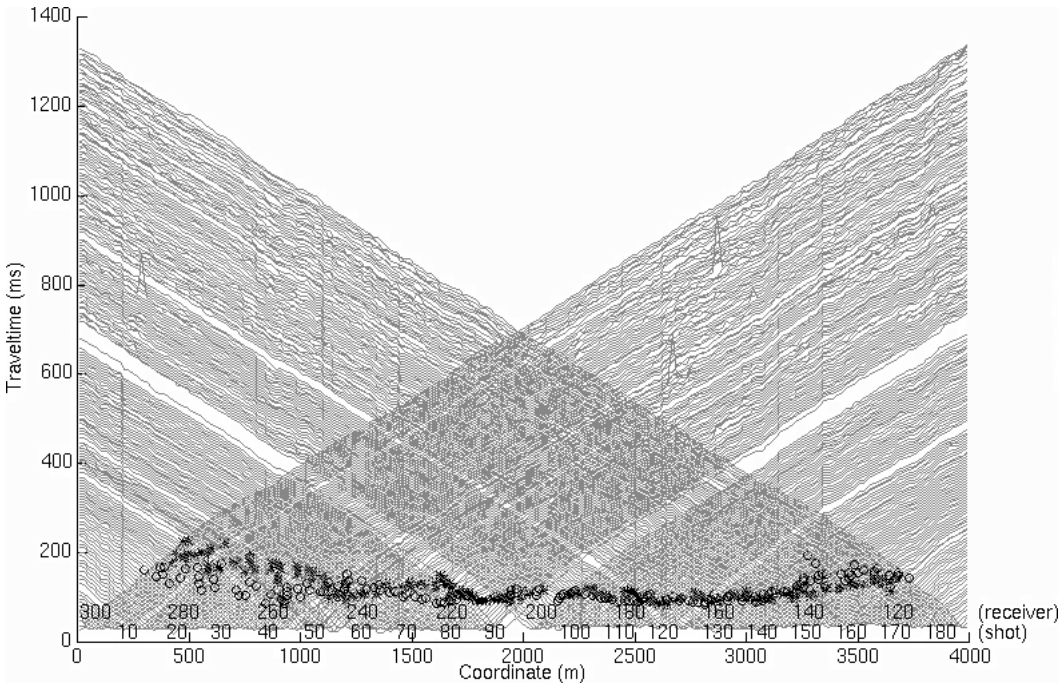

Figure 15. Crossover point averages of the *P*-wave refractions for the left trailing (o) and right leading (*) shot spreads.

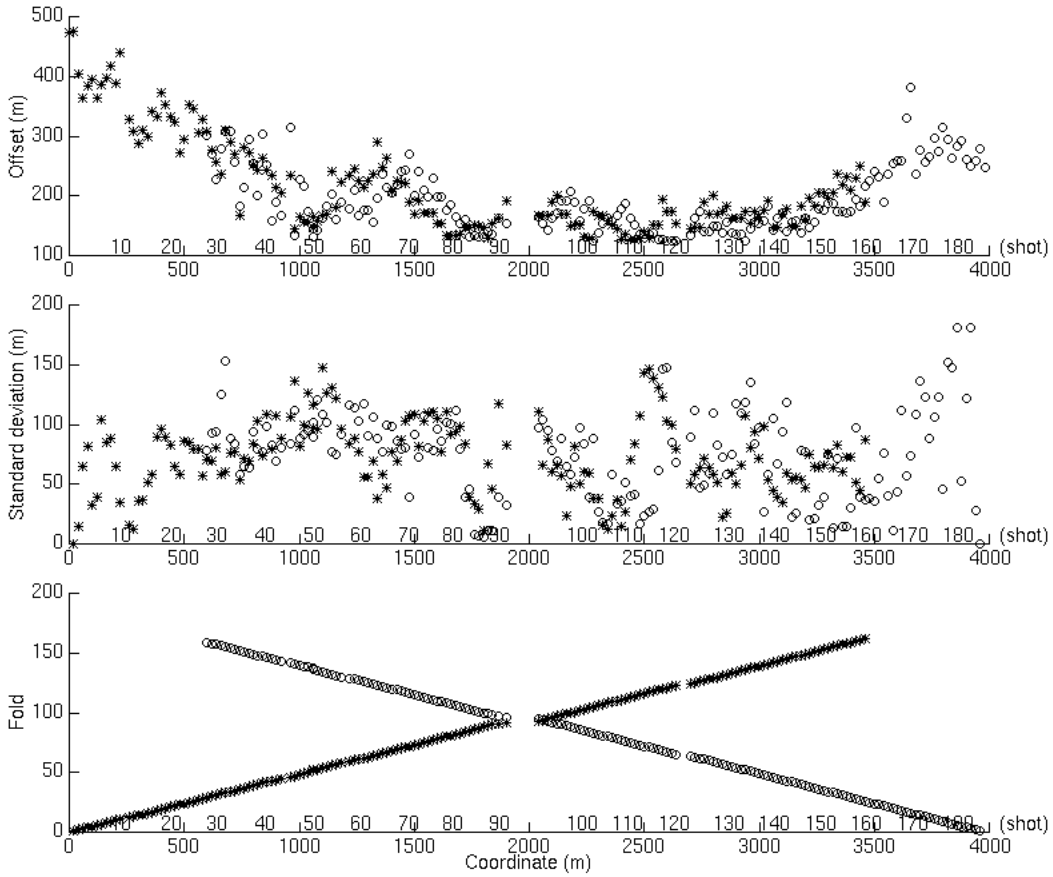

Figure 16. Display of the right crossover point average (*) and left crossover point average (o) for the *P*-wave refractions.

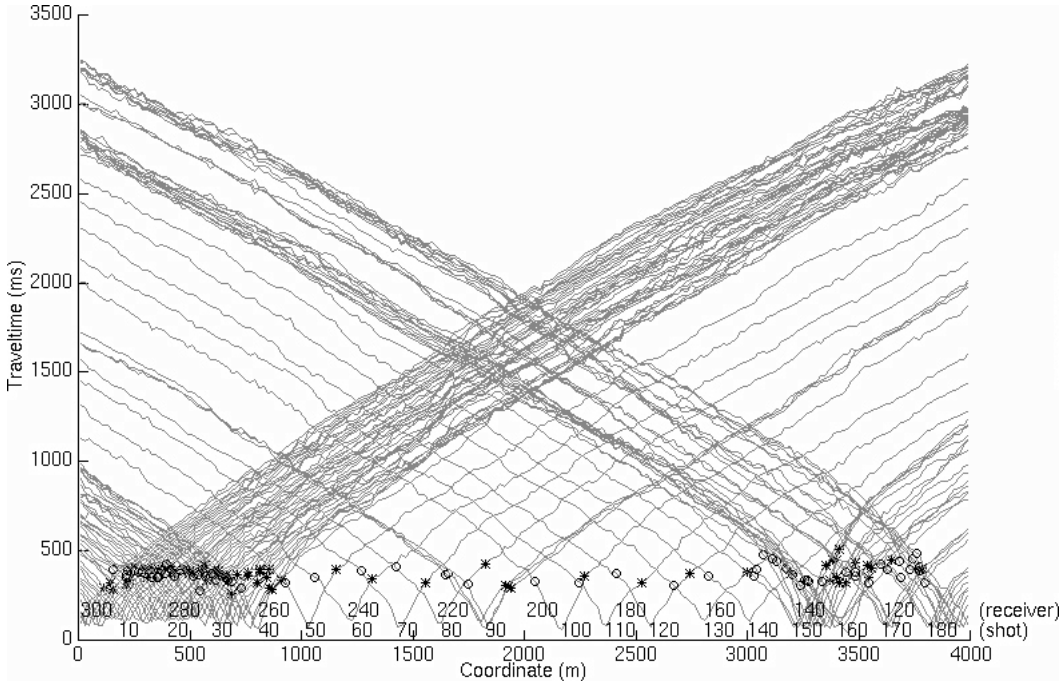

Figure 17. Crossover point averages of the *S*-wave refractions for the left trailing (o) and right leading (*) shot spreads.

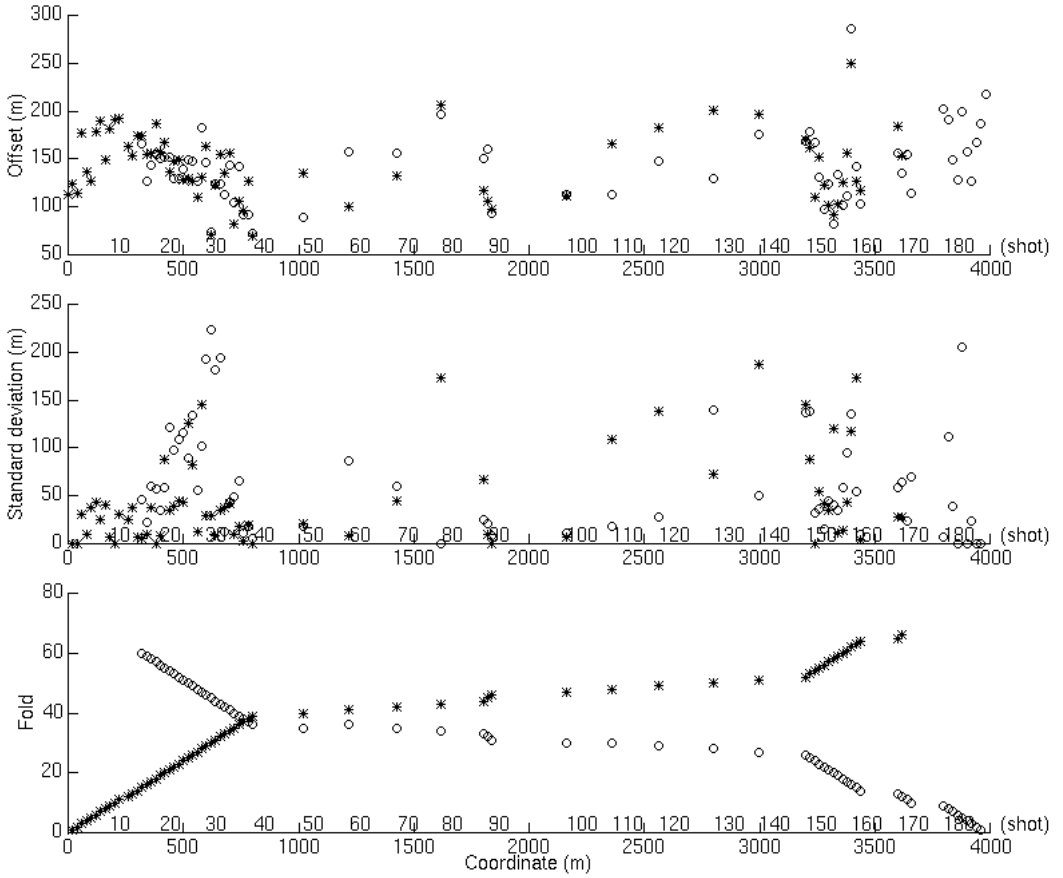

Figure 18. Display of the right crossover point average (*) and left crossover point average (o) of the *S*-wave refractions.

Velocity model

The velocity model can be established with the knowledge of the crossover point average locations. The velocity calculation process uses the direct arrival traveltimes (from shot to crossover point location) to find the velocity of the subweathering layer and the refracted arrival traveltimes (from the crossover point location to the end of survey or to an arbitrate offset limit) to establish the second layer velocity (Minus time analysis). Figures 19 and 20 show respectively the velocity models from the *P*-wave arrivals and *S*-wave arrivals. A median filter (window length of 7 samples) was applied on both model to reduced the short wavelength variation. The average *P*-wave velocities for the first and second layer are respectively 1968 m/s and 3006 m/s, while the average *S*-wave velocity for the first layer is 465 m/s and 1181 m/s for the second layer. The first layer *P*-wave velocity increases at both ends of the survey. The increase of the *P*-wave velocity coincides with an increase of the crossover point offsets The V_p/V_S ratio is 4.2 for the first layer and 2.5 for the second layer.

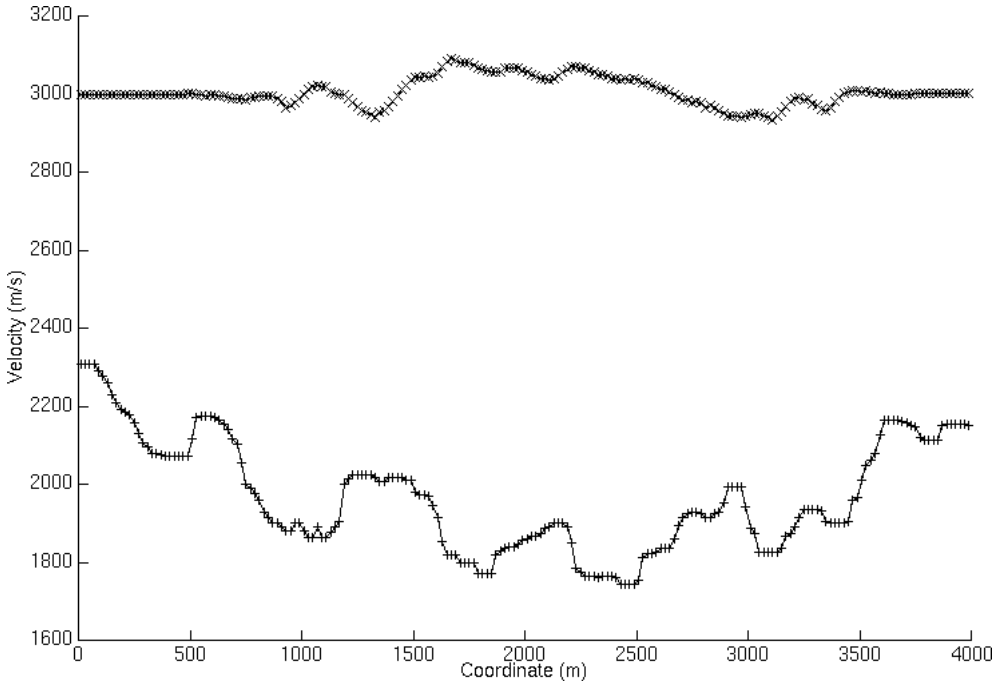

Figure 19. *P*-wave velocity model calculated from the *P*-wave arrival traveltimes: first layer velocity (+) and second layer velocity (x). Both velocities were median filtered with a window length of 7 samples.

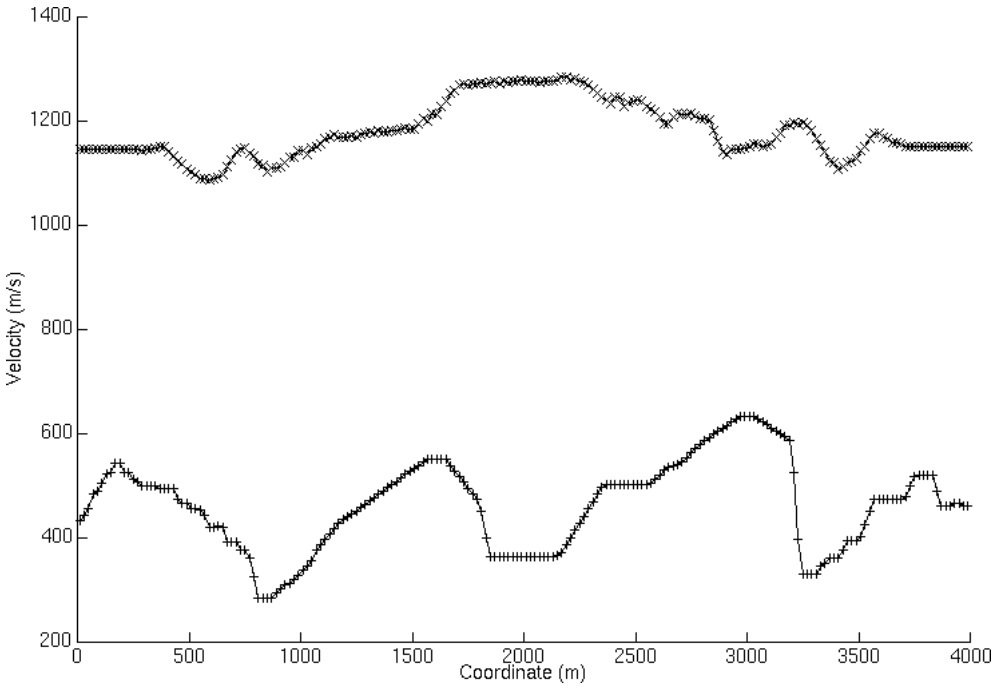

Figure 20. *S*-wave velocity model calculated from the *S*-wave arrival traveltimes: first layer velocity (+) and second layer velocity (x). Both velocities were median filtered with a window length of 7 samples.

Plus time and delay time analyses

The Plus time analysis process was undertaken on both *P*-wave and *S*-wave refractions according to the respective crossover point average locations and a user-selected offset limit. An offset limit of 3000 meters, which constrained the Plus-Minus time analysis window, was used to remove suspected third layer refracted arrivals from the computation. The Plus Time for each receiver location is defined as the sum of the traveltime at the receiver from a forward shot and the traveltime at the same receiver from a reverse shot, minus the total traveltime between these shots. Figure 21 shows the Plus Time average values at each receiver with the corresponding statistics (standard deviation and fold) for the *P*-wave refractions, while figure 22 shows the results for the *S*-wave refractions. The standard deviation increases abruptly at both extremity of the survey because the delay time analysis was used in replacement of the Plus time analysis, which is limited by the Plus-Minus time analysis window. The delay times for the receivers outside the Plus-Minus time analysis window are found using the shot delay times, which are calculated from the known Plus Time values of receivers at the same locations (Lawton, 1989). The fold at the survey extremities is less than at the other surface locations because the delay time analysis uses only one shot spread at a time while Plus time analysis uses all the possible combinations of two shot spreads.

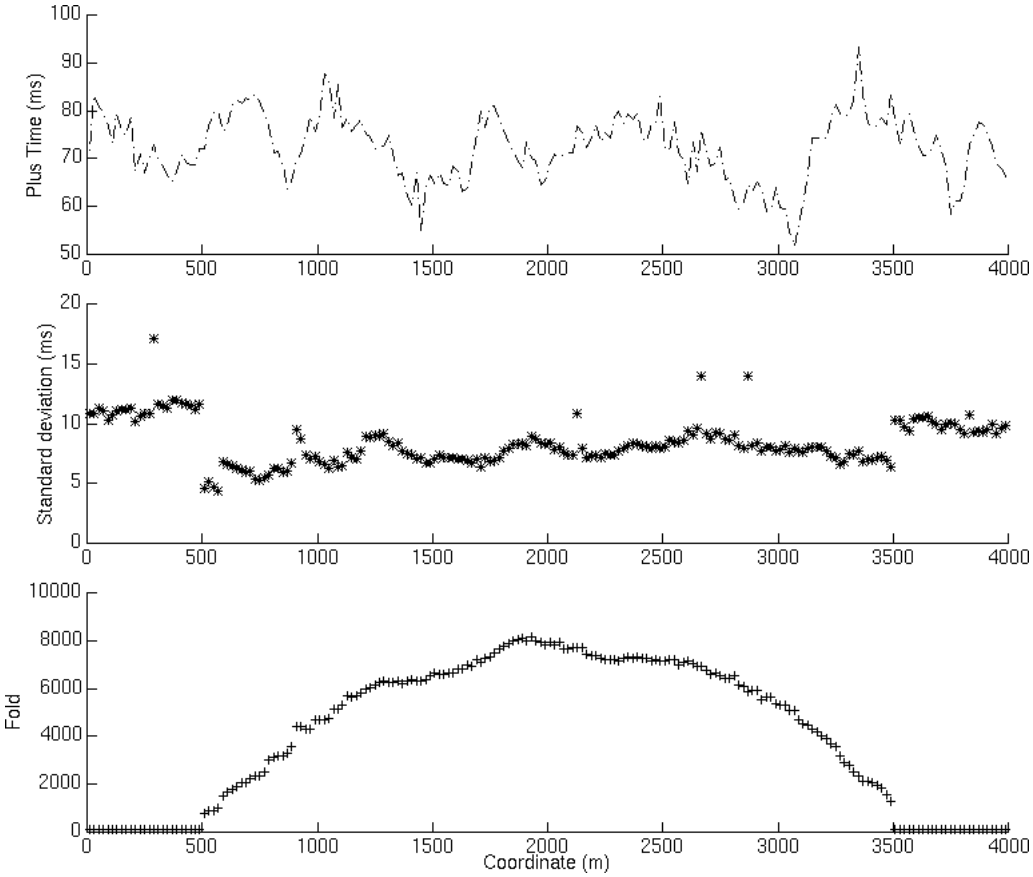

Figure 21. Plus Time values and statistics for the *P*-wave refractions.

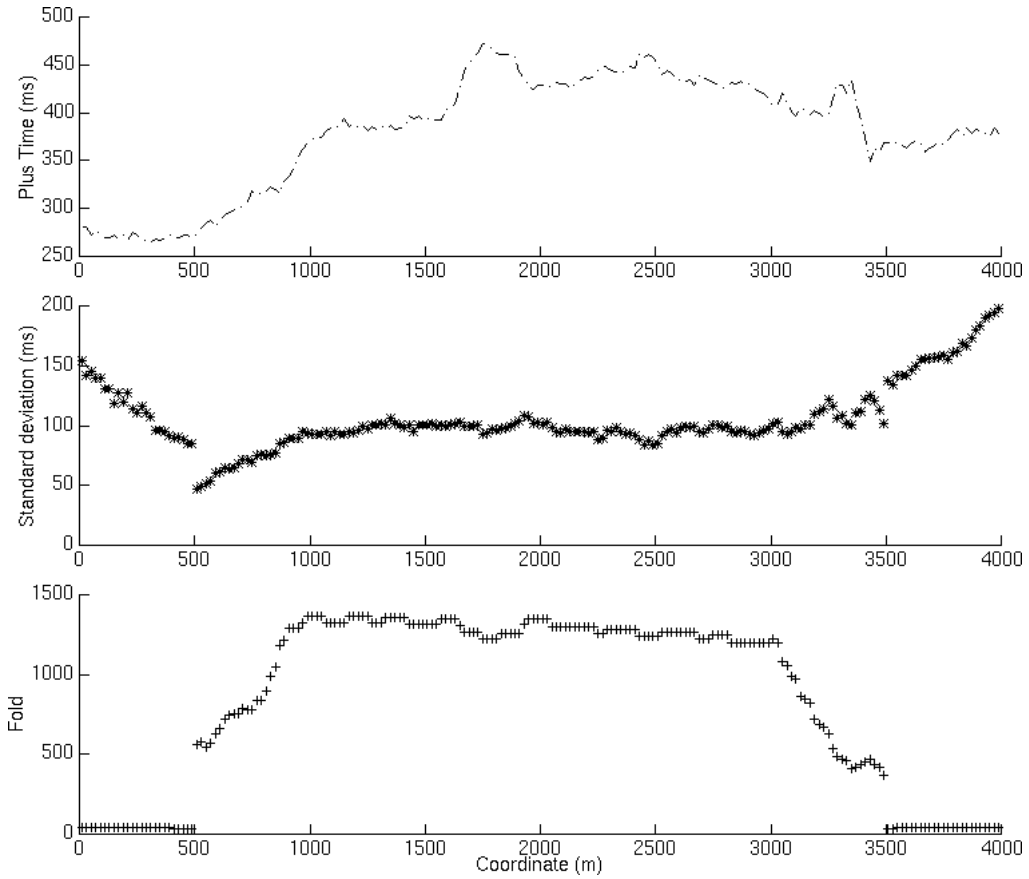

Figure 22. Plus Time values and statistics for the *S*-wave refractions.

Depth model

The first layer thickness calculations were undertaken using the velocities and the Plus Time values. For the *P*-wave and *S*-wave depth model calculations, constant first layer velocity of 1968 m/s and 465 m/s, respectively, were used instead of the calculated velocities to reduce the short wavelength variation due to arrival picking errors and lack of receiver coverage in the near-offset. Figure 23 shows the *P*-wave depth model and the corresponding statistics (standard deviation and fold), while figure 24 displays the *S*-wave model. The average thickness of the first layer is of 94 m for the *P*-model and of 96 m for the *S*-model. In both cases, the first layer includes the thin surficial glacial deposits and shale. The second layer which has a *P*-wave velocity of about 3000 m/s and *S*-wave velocity of about 1200 m/s is probably composed of a more compacted and coarser-grained sandstone of the Paskapoo Formation.

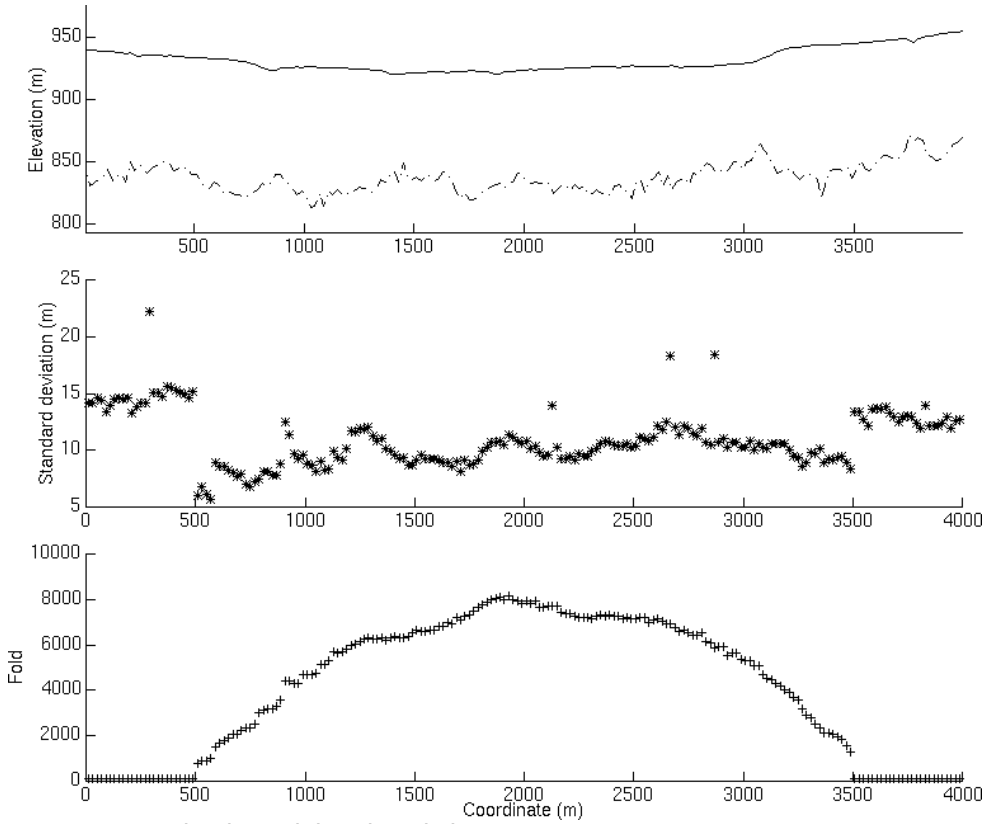

Figure 23. *P*-wave depth model and statistics.

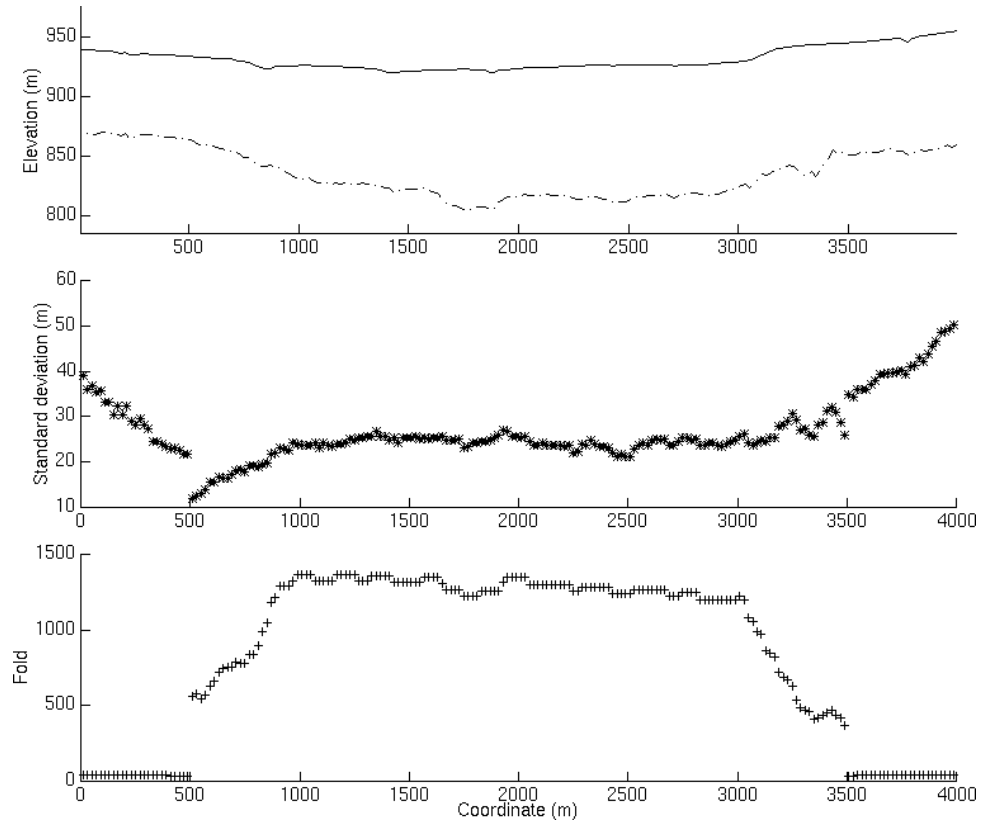

Figure 24. *S*-wave depth model and statistics.

Static corrections

With the *P*-wave and *S*-wave models (depths and velocities) known, the static corrections were computed. Figures 25 and 26 show the surface-consistent elevation corrections, weathering corrections and total corrections for the *P*-wave model and *S*-wave model. The datum elevation used was 930 m, which is the average surface elevation. The replacement velocity was 3100 m/s for the *P*-wave model and 1200 m/s for the *S*-wave model. In both cases, a pseudo-datum was used to minimize the influence of the replacement velocity choice. The pseudo-datum corresponds to the deepest elevation of the first and second layer interface, which is 812 m for the *P*-wave model and 805 m for the *S*-wave model.

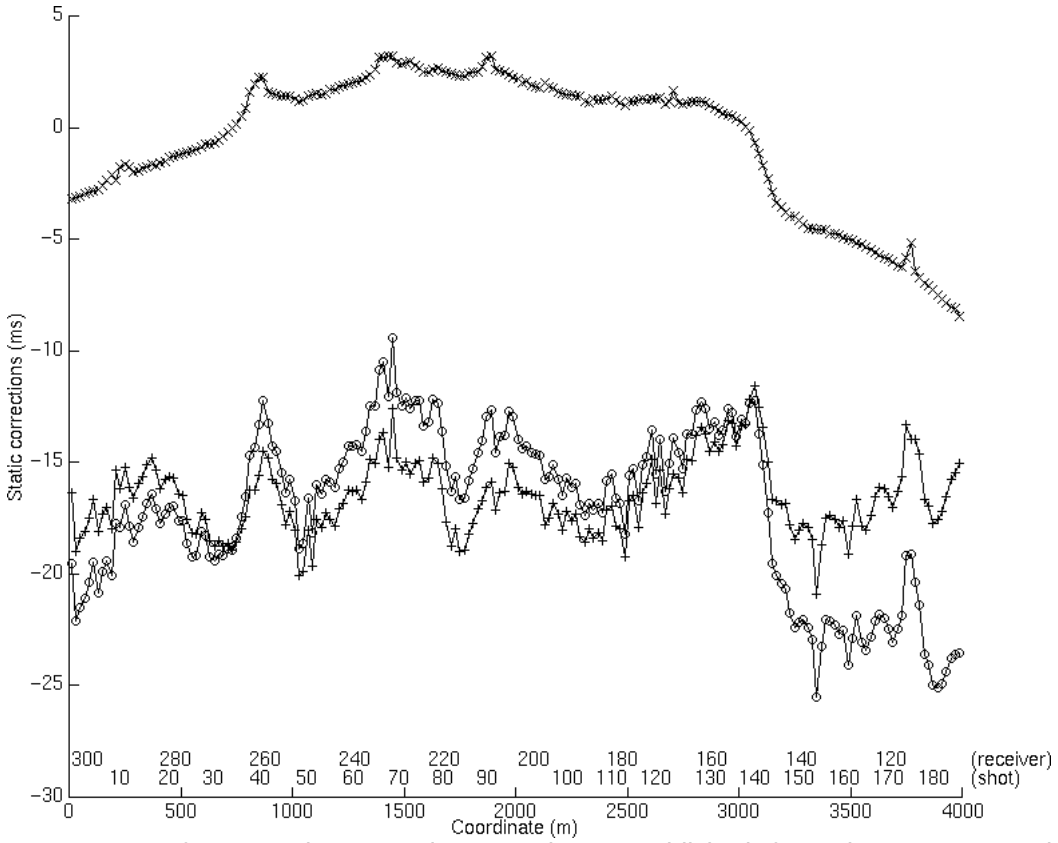

Figure 25. Surface consistent static corrections established from the *P*-wave model: elevation corrections (*), weathering corrections (+), and total corrections (o).

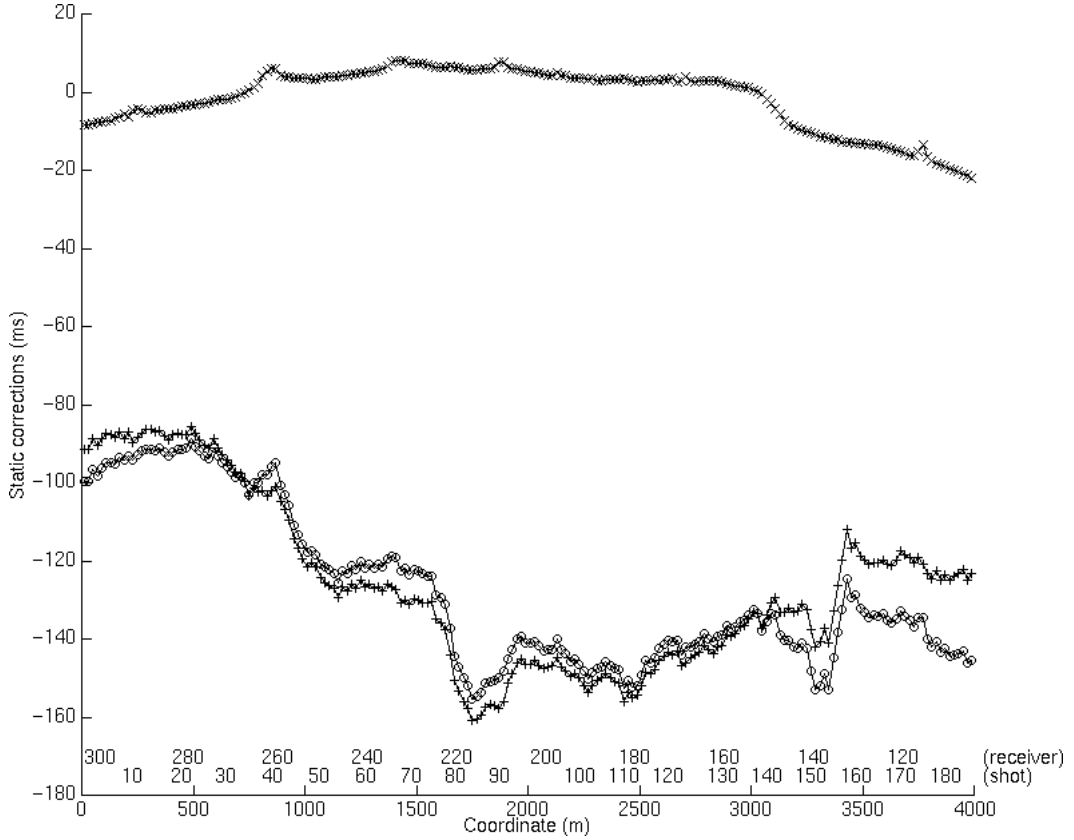

Figure 26. Surface consistent static corrections established from the *S*-wave model: elevation corrections (*), weathering corrections (+), and total corrections (o).

GENERALIZED LINEAR INVERSION METHOD

The Generalized Linear Inversion (GLI) method by Hampson and Russell (1984) uses an input model an its calculated refracted traveltimes to compare and to match them with the observed refracted traveltimes by updating the model iteratively.

Initial input model

The first step of the Generalized Linear Inversion method is to build an approximate near-surface model. The model is built using a slope picking process of the refracted arrivals in an offset window. The same refracted arrival traveltimes (*P* and *S*) used for the Plus-Minus time analysis method were used to build the *P*-wave and *S*-wave input model. Figure 27 displays all the *P*-wave refracted arrival traveltimes in term of offset, as well as the initial input model (straight line-slope). The initial *P*-wave model has a first layer velocity of 1968 m/s and a second layer velocity of 3168 m/s. The initial first layer thickness is of 95 meters, according to the intercept time of 76 ms. Similarly, the *S*-wave refracted arrival traveltimes with the initial input model (straight line-slope) are shown in figure 28. The initial *S*-wave velocities are 465 m/s and 1325 m/s for the first and second layer, respectively. The initial first layer thickness is of 87 meters (intercept time of 350 ms).

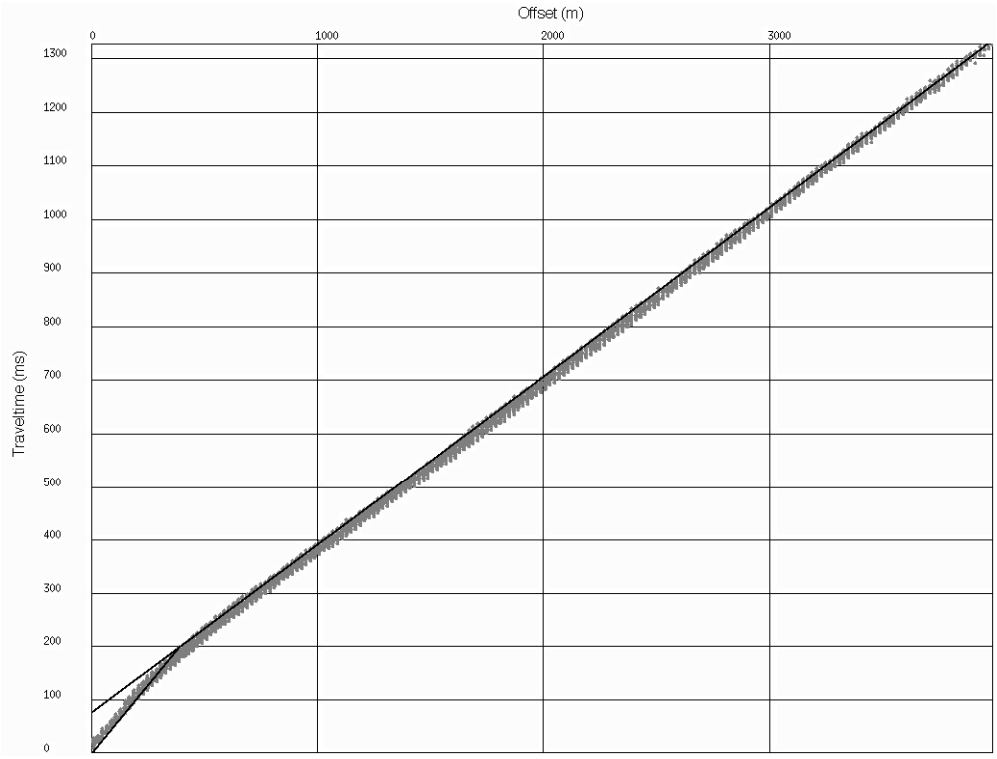

Figure 27. *P*-wave refracted arrival traveltimes versus offset and initial input *P*-wave model (straight line-slope).

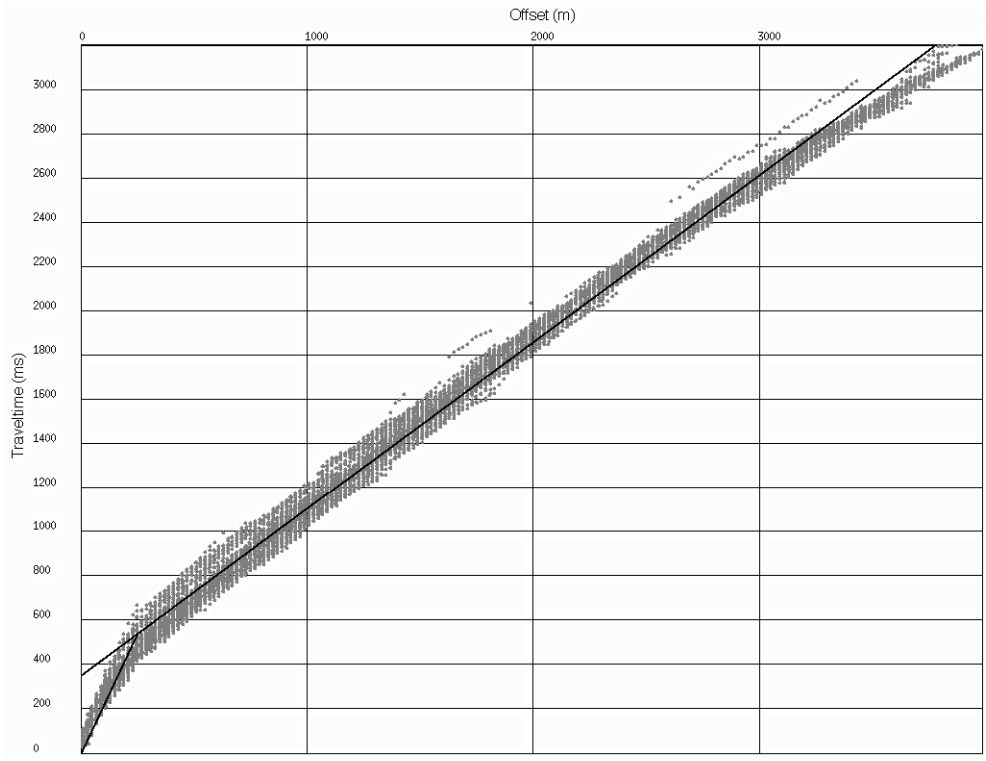

Figure 28. *S*-wave refracted arrival traveltimes versus offset and initial input *S*-wave model (straight line-slope).

Final inverted model

From the initial input models (*P* and *S*), arrival traveltimes are calculated using a simple raytracing method (straight raypath and locally flat layer). The inversion procedure consists of sequentially modifying the thickness and velocity of the input model to get a closer match of the calculated arrival traveltimes with the observed arrival traveltimes (Gauss-Seidel iteration and conjugate-gradient algorithm). Like with the Plus-Minus time analysis, an offset limit of 3000 meters was used to remove suspected third layer arrivals, which can easily be seen in figure 28. To stabilize the inversion, a depth smoother of 150 meters and a velocity smoother of 1500 meters were used. The result of the inversion on the *P*-wave and *S*-wave model is expressed in term of variation in the first layer thicknesses and second layer velocities. The average thickness of the inverted *P*-wave depth model is 93 meters and the average second layer velocity is 3190 m/s, while the first layer velocity remains unchanged. The average thickness of the first layer for the *S*-wave model is 91 meters and the second layer velocity average is 1289 m/s.

COMPARISON OF PLUS-MINUS TIME ANALYSIS METHOD AND GENERALIZED LINEAR INVERSION METHOD RESULTS

Depth model comparison

The *P*-wave and *S*-wave depth models can be compared by looking at the elevation of the first and second layer interface. Figure 29 shows the elevation of the first and second layer interface of the *P*-wave depth model for the Plus-Minus time analysis (PMT) and Generalized Linear Inversion (GLI) methods, whereas figure 30 displays the elevation of the first and second layer interface of the *S*-wave model for the two methods. The elevation average for the *P*-wave depth model is 837 meters with the PMT method and 838 meters with the GLI method, while the elevation average for the *S*-wave depth model is 835 meters with the PMT method and 841 meters with the GLI method. When comparing the interface elevations for the *P*-wave models, it is noticed that GLI elevations track the PMT elevations. The GLI elevations are smoother due to the depth smoother used (150 meters). If we look at the *S*-wave interface elevations, the PMT and GLI elevations have the same shape, although there is a constant elevation difference in the middle of the survey line and greater elevation differences for the PMT interface.

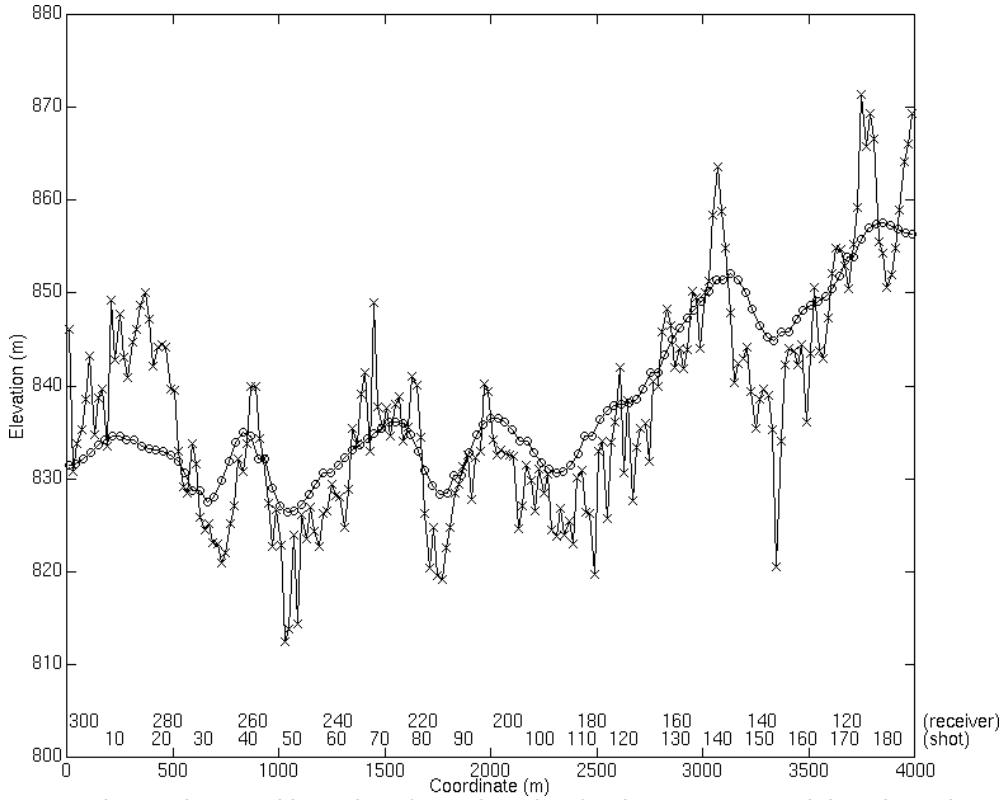

Figure 29. First and second layer interface elevation for the *P* -wave models: Plus-Minus time analysis method (x) and Generalized Linear Inversion method (o).

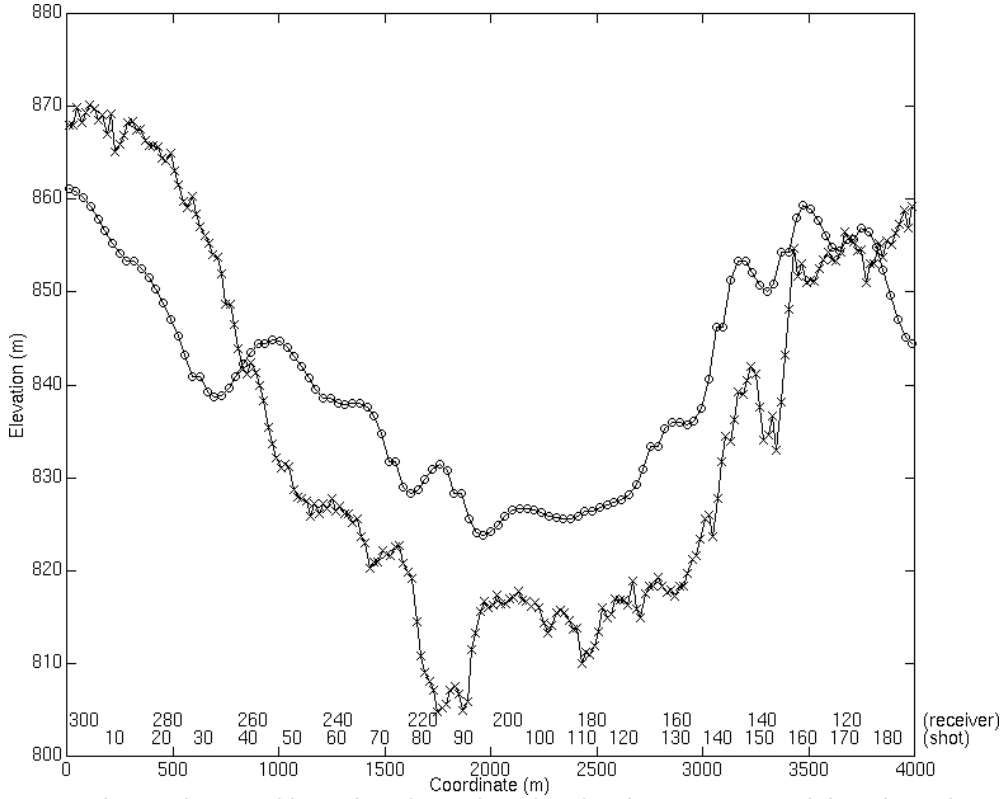

Figure 30. First and second layer interface elevation for the*S* -wave models: Plus-Minus time analysis method (x) and Generalized Linear Inversion method (o).

Static solution comparison

From the *P*-wave and *S*-wave models, the static corrections were computed. The datum used for both PMT and GLI models was 930 meters. The replacement velocity for the *P*-wave models was 3100 m/s and 1200 m/s for the *S*-wave models. The receiver static corrections calculated from the *P*-wave models (PMT and GLI) are shown in figure 31. The two solutions are very similar in term of long wavelength character. Figure 32 displays the receiver static corrections for the *S*-wave models (PMT and GLI). Again, both solutions express the same features with a constant difference of about 20 ms in the middle of the survey line (receiver number 135-250). However, difference are noticed between the PMT and GLI static solutions at the beginning and at the end of the survey line. The receiver static corrections coming from the *P*-models can be applied to the vertical component data, while the receiver static corrections calculated from the *S*-models are for the radial component data. The shot static corrections computed from the *P*-models are used for both vertical and radial component data. Figure 33 shows the shot static corrections established from the *P*-models and the shot hole depth. Both PMT and GLI solutions have similar values with some differences in terms of intermediate and high frequencies statics.

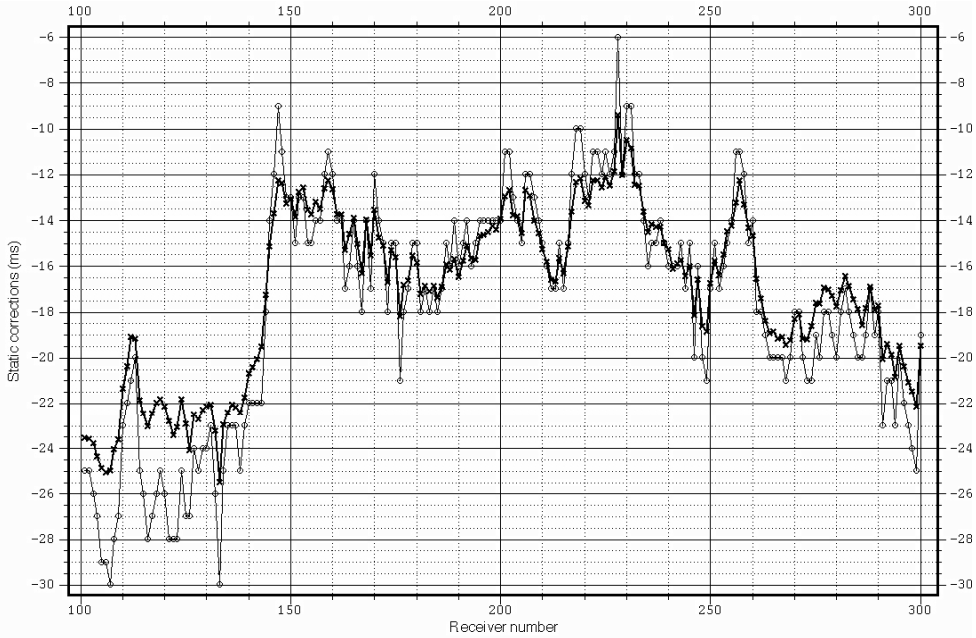

Figure 31. Receiver static corrections (weathering + elevation) from the *P*-models: PMT (x) and GLI (o).

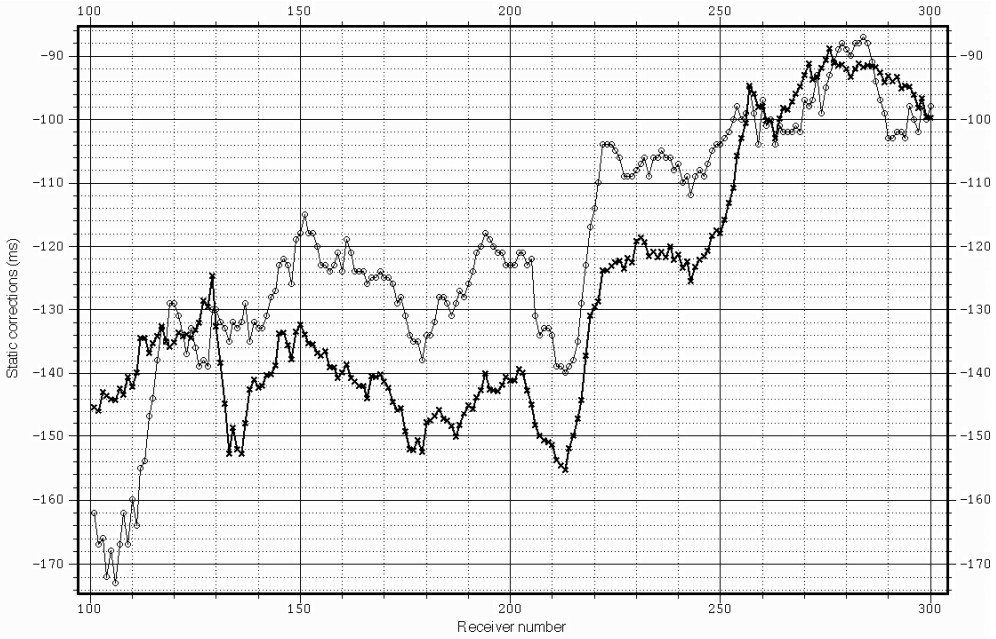

Figure 32. Receiver static corrections (weathering + elevation) from the *S*-models: PMT (x) and GLI (o).

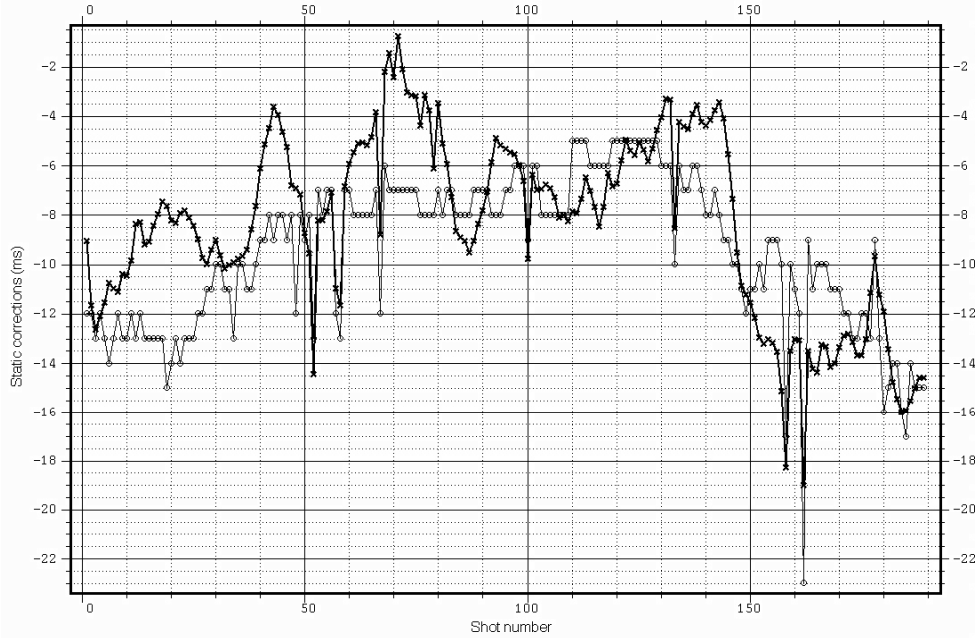

Figure 33 Shot static corrections (weathering + elevation) from the *P*-models: PMT (x) and GLI (o).

Common receiver stack comparison

Common receiver stacks were produced using the vertical and the radial component. As explained previously, the shot static corrections calculated from the *P*-models (PMT and GLI) are used in combination of the receiver static corrections calculated from the *S*-models (PMT and GLI) to establish the total static corrections to be applied to the radial component traces. The quality of a common receiver stack and the efficiency of the static corrections applied can be determined looking at the reflector structure and continuity (receiver static corrections), as well as the energy focus (shot static corrections). Figures 34, 35 and 36 show respectively the vertical component common receiver stacks without any static correction, with the PMT static solutions and GLI static solutions applied. Both common receiver stacks with the PMT and GLI static solutions show clear improvement compared to the common receiver stack without static corrections. The static corrections have successfully remove the false reflector time structure, enhanced the reflector continuity, and have provided better energy focus. Both PMT and GLI solutions give comparable results.

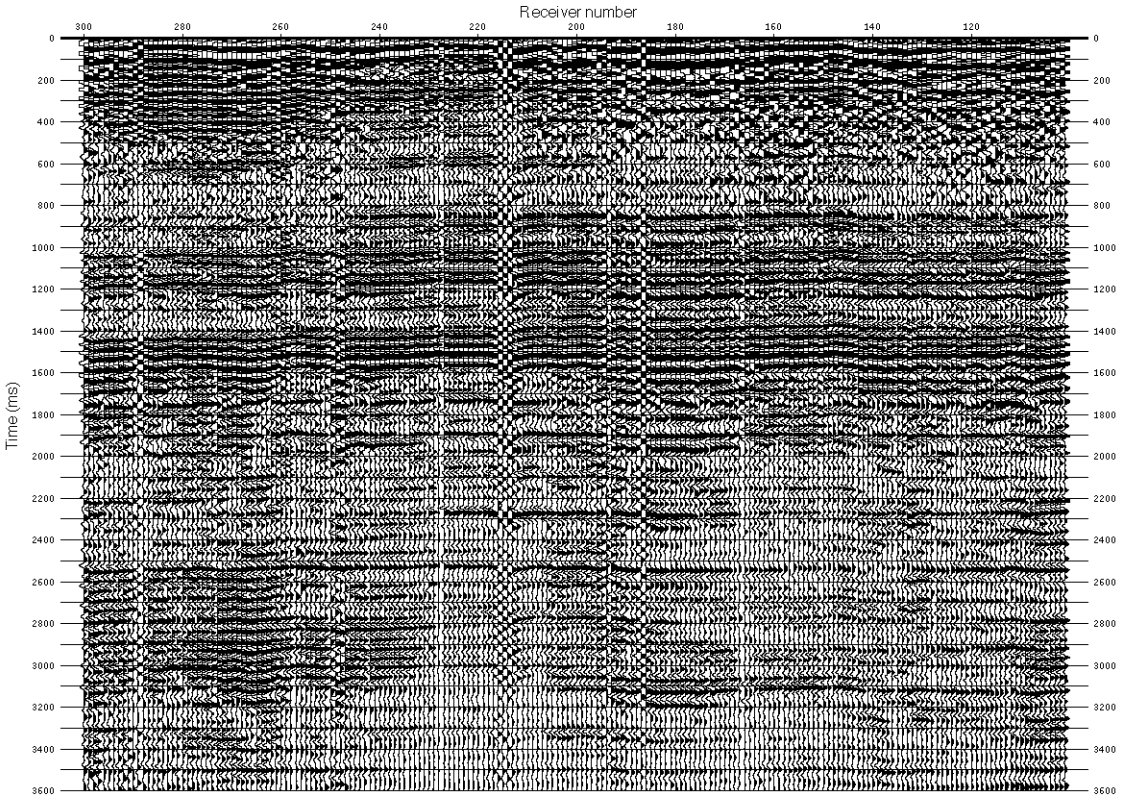

Figure 34. Vertical component common receiver stack (raw).

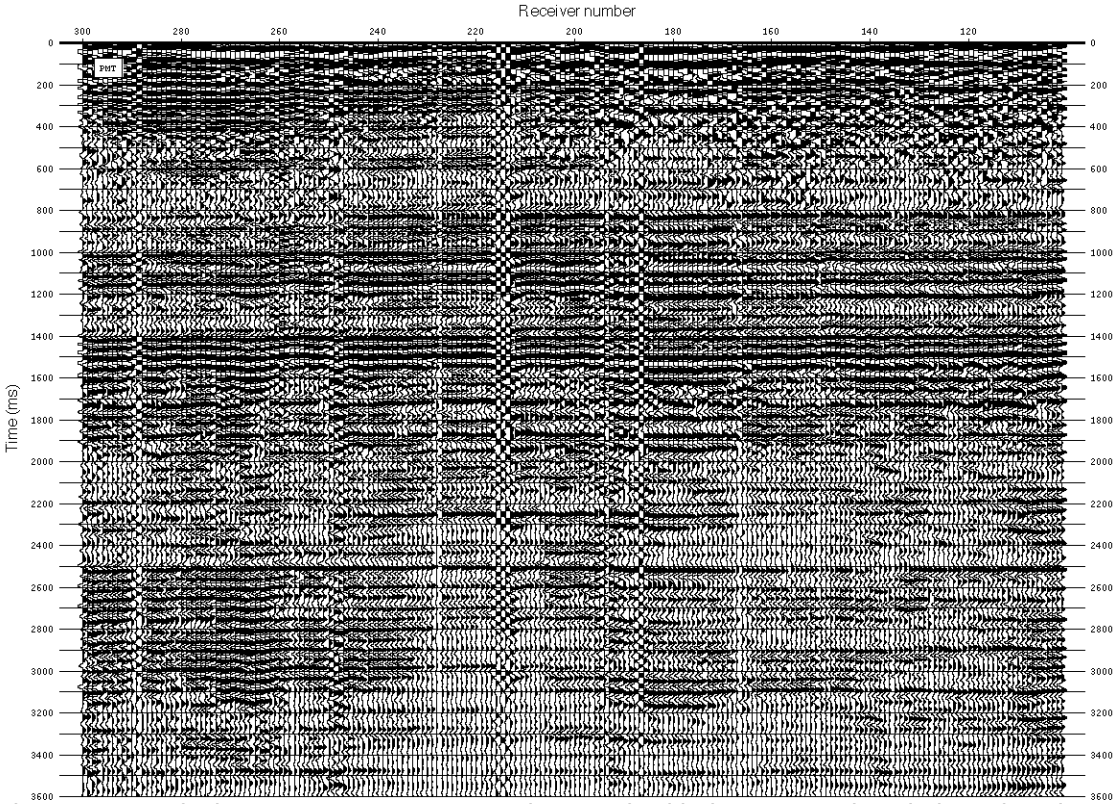

Figure 35. Vertical component common receiver stack with the PMT static solutions (receiver and shot static corrections from the PMT *P*-model).

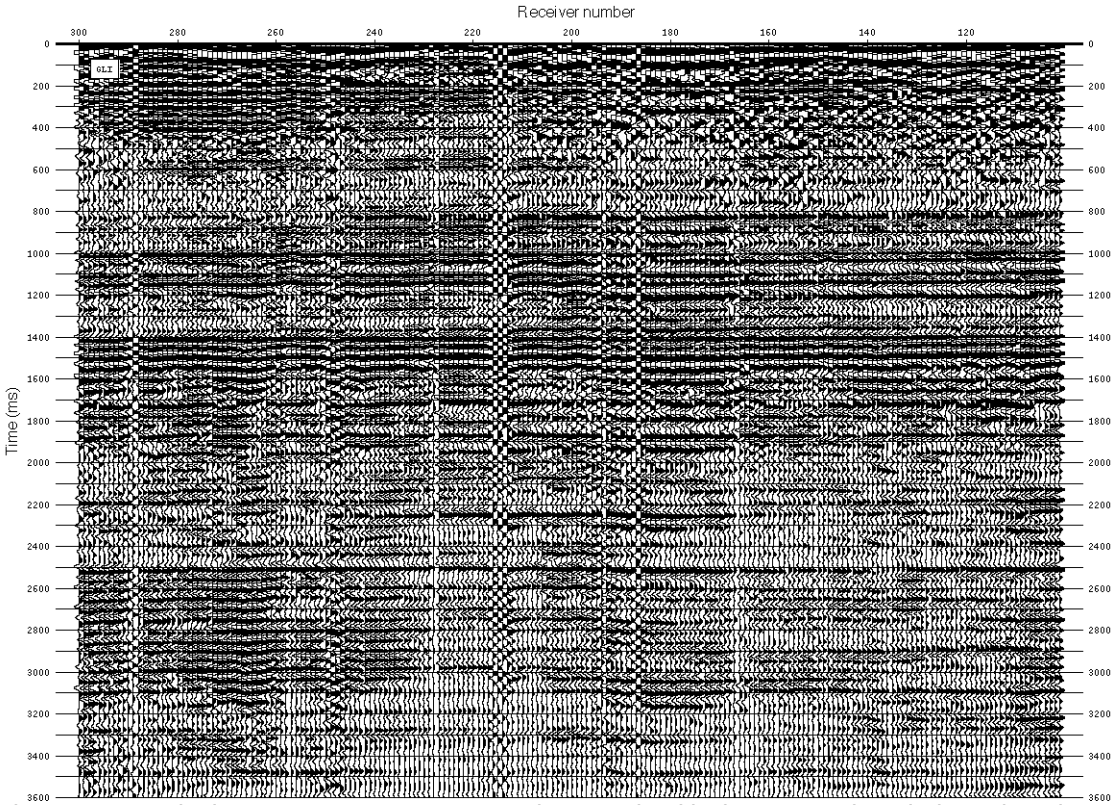

Figure 36. Vertical component common receiver stack with the GLI static solutions (receiver and shot static corrections from the GLI *P*-model).

Figures 37, 38 and 39 show respectively the radial component common receiver stacks without static correction, with the PMT static solutions and GLI static solutions applied. There is an improvement to the common receiver stack with the PMT and GLI static solutions applied in comparison with the raw common receiver stack. The static corrections did remove some false reflector time structure and enhance the reflector continuity. However, the improvement is not as obvious and significant as the improvement on the vertical component, also the PMT and GLI static solutions both seem to have added some long wavelength reflector structure. Figure 40 displays a reflector horizon before and after the static solutions were applied. It can be noticed that a reflector structure is being added in the middle of the survey line, around receiver number 210, which corresponds to an increasing thickness feature in the PMT *S*-wave model in between coordinate 1500 to 2000 meters (receiver number 200-230, see figure 30). This feature has a thickness of about 10 meters and is believed to be a paleochannel. It is possible that the *P-S* reflections were not affected by this local channel feature like the *S*-wave refractions. This can be explained if the channel is filled with the same material of the second layer (sand), so that the reflection are not affected by the channel. The *S* head-wave, instead of following the shale-sandstone interface, may follow the bottom of the channel feature. The increasing static correction values (PMT and GLI) towards the middle and the end of the survey line are due to an increasing first layer thickness trend. Therefore, a long wavelength time structure trend is being added to the reflector. However, removal of some intermediate wavelength apparent-reflector structure has been achieved, especially along the first half of the survey line. Difference between the reflector structure with the PMT static solutions and the reflector structure with the GLI static solutions is less obvious. The PMT static solutions give a better result at the end of the survey line between coordinate 3500 to 4000 meters (receiver number 101-130).

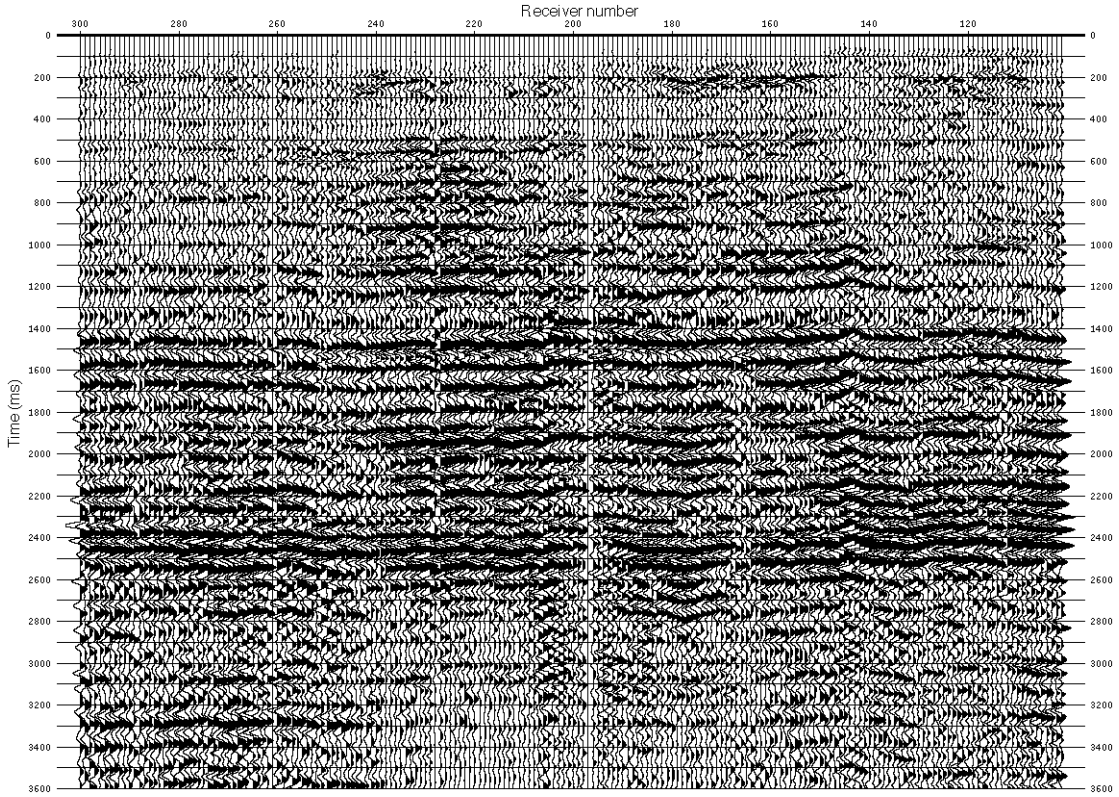

Figure 37. Radial component common receiver stack (raw).

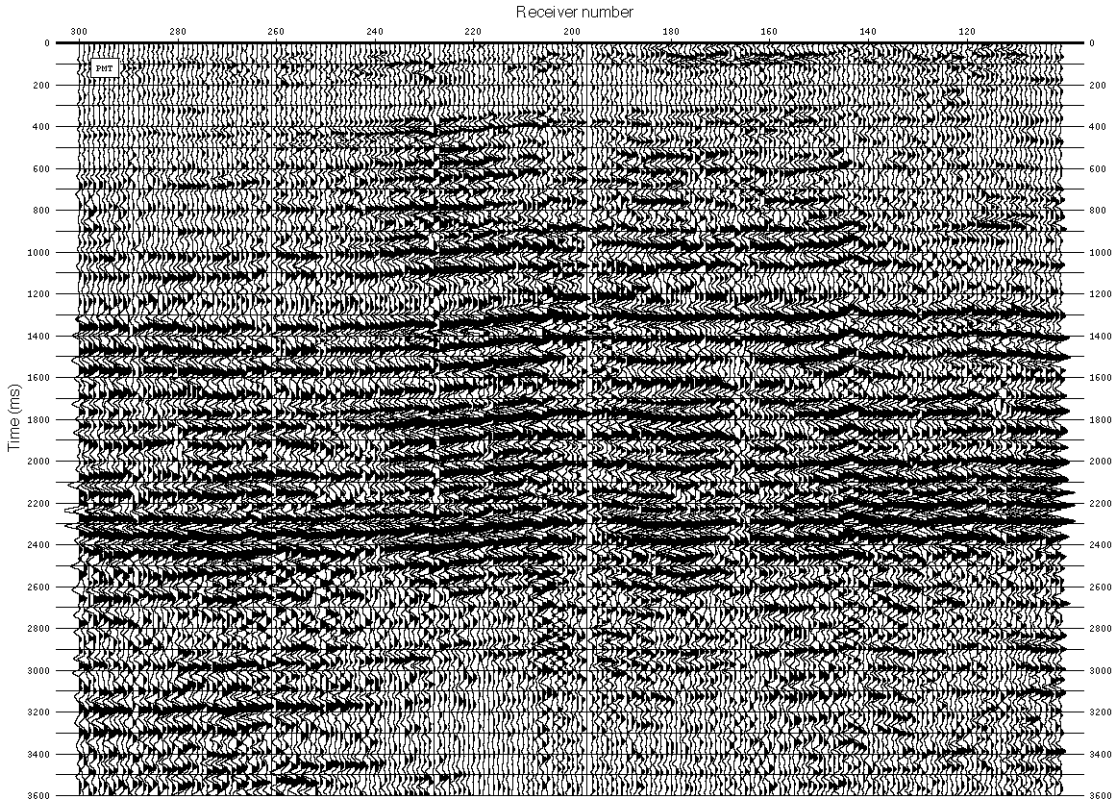

Figure 38. Radial component common receiver stack with the PMT static solutions (receiver static corrections from the PMT *S*-model and shot static corrections from the PMT *P*-model).

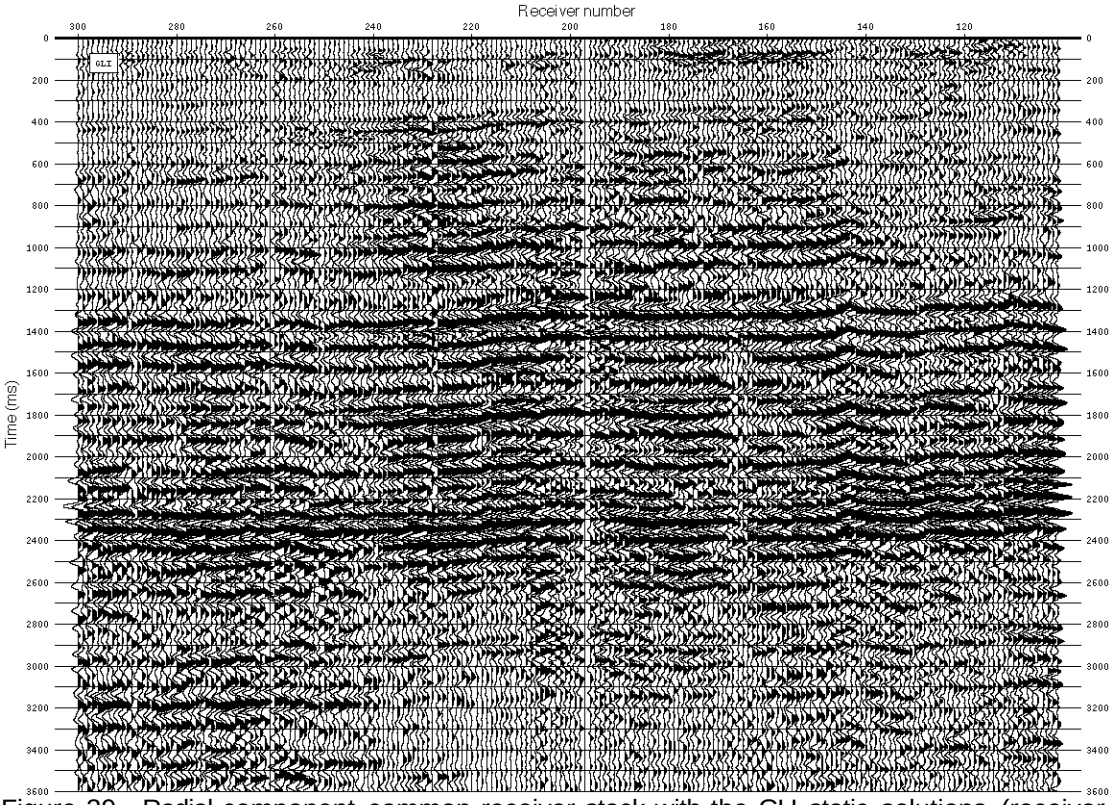

Figure 39. Radial component common receiver stack with the GLI static solutions (receiver static corrections from the GLI *S*-model and shot static corrections from the GLI *P*-model).

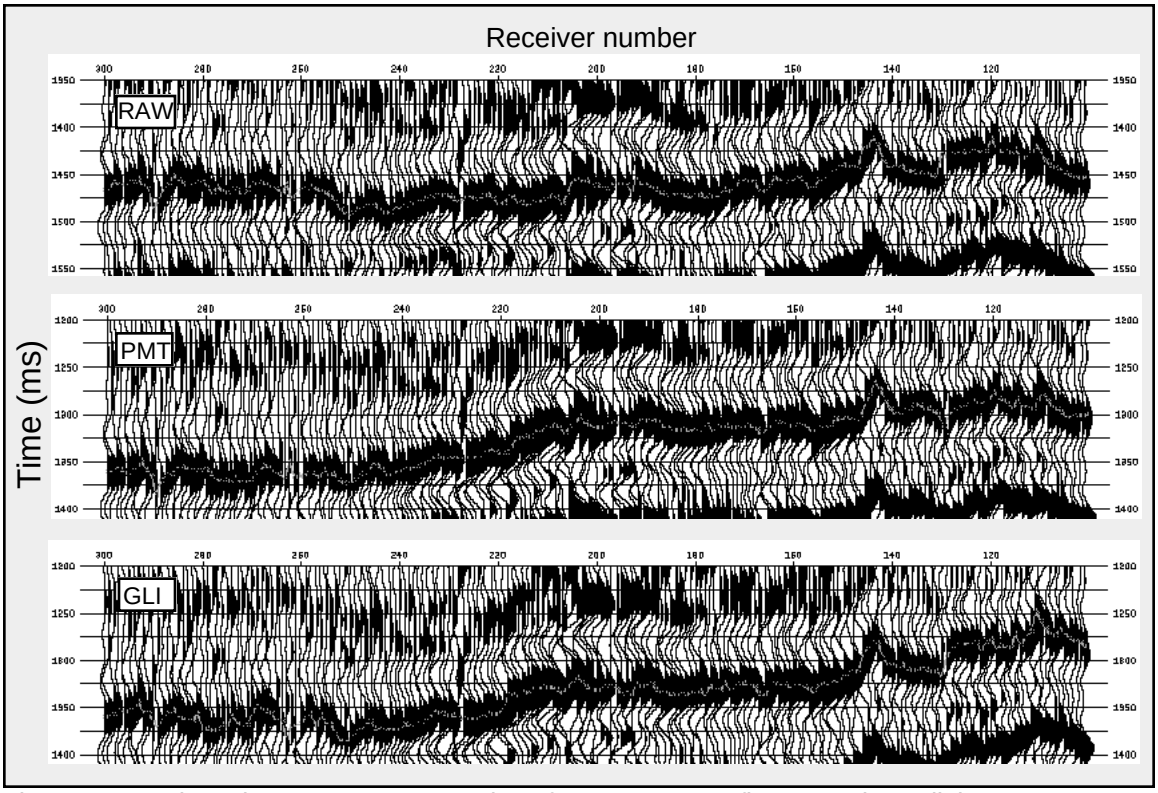

Figure 40. Horizon time structure comparison for a common reflector on the radial component data before and after static corrections applied (PMT and GLI static solutions).

CONCLUSION

S-wave refractions were identified on the radial component of the Blackfoot 2D-3C dataset and were used to establish a *S*-wave near-surface model, while *P*-wave refraction were used to build the *P*-wave model. Two refraction methods were used: the Plus-Minus time analysis method and the Generalized Linear Inversion method. The average first layer thickness for both *P* and *S*-wave near-surface model was established at 94 meters, which correspond to a combination of thin glacial deposits and shale. The average *P*-wave velocity for the first layer is 1968 m/s and around 3100 m/s for the second layer, while the average *S*-wave velocity is 465 m/s for the first layer and around 1200 m/s for the second layer. The V_P/V_S ratio of the first layer is 4.2 and 2.5 for the second layer. According to the *P*-*S* reflection raypath geometry (downgoing *P*-wave and upgoing *S*-wave), the shot static corrections were computed from the *P*-wave model and the receiver static correction from the *S*-wave model and were applied to the radial component data. Some improvements were noticed in term of intermediate wavelength reflector structure and reflector continuity. However, the improvement is not as clear as with the application of the static corrections (*P*-wave shot and receiver static corrections) on vertical component. The use of static corrections based on the near-surface models (*P* and *S*) instead of hand picking correction remains more meaningful and physically realistic. The results of the Plus-Minus time analysis and Generalized Linear Inversion methods are consistent in term of depths, velocities, static corrections. However, due to smoothing filters required for the inversion, the Plus-Minus time analysis method provides a more detailed model than Generalized Linear Inversion method in terms of depths and velocities. The Plus-Minus time analysis model solutions (depth and velocity) are strictly based on the refracted arrivals, whereas the Generalized Linear Inversion model solutions depend on the input model and the smoothing filters.

REFERENCE

Anno, P. D., 1986, Two critical aspects of shear-wave analysis: Statics solutions and reflection correlations, in Danbom, S. H., and Domenico, S. N., Eds., Shear-wave exploration: Soc. Expl. Geophys. Dev. Series, 1, p. 48-61.

Cary, P. W., and Eaton D. W. S., 1993, A simple method for resolving large converted-wave (*P-SV*) statics: Geophysics, v.58, p. 429-433.

Dufour, J., and Foltinek, D. S., 1996, Plus-Minus time analysis method and its implementation, chapter 13, CREWES Research Report, vol.8, 1996.

Edelmann, H. A. K., and Helbig, K., 1988, Shear-wave surveys- some aspects of field layout, in Danbom, S. H., and Domenico, S. N., Eds., Shear-wave exploration: Soc. Expl. Geophys. Dev. Seiries, 1, p. 39-47.

Geiger, K. W., 1967, Bedrock topography of the Gleichen area, Department of Energy, Mines and Resources, Ottawa.

Hagedoorn, J. G., 1959, The Plus-Minus method of interpreting seismic refraction sections, Geophysical Prospecting 7, p. 158-182.

Hampson, D., and Russell, B., 1984, First break interpretation using generalized linear inversion: J. Soc. Expl. Geophys., 20, p. 40-54.

Irish, E. J. W., 1967, Geology map of Gleichen area, Institute of Sedimentary and Petroleum Geology, Geological Survey of Canada.

Jolly, R. N., and Mifsud, J. F., 1971, Experimental studies of source generated noise: Geophysics, v.36, p. 1138-1149.

Lawton, D. C., 1989, Computation of refraction static corrections using first-break traveltime differences: Geophysics, v.54, p. 1289-1296.

Stalker, A. Macs., Surficial geology of High River area, Geological Survey of Canada.

Teller, J. T., and Clayton, L., 1983, Glacial Lake Agassiz: Geological Association of Canada, Special Paper 26, 451 p.

Thornburgh, H. R., 1930, Wave-front diagrams in seismic interpretation, Bulletin of the American Association of Petroleum Geologists 14, p. 185-200.

Wang, W., and Cheadle, S., 1995, Branch point analysis in refraction interpretation, CSEG National Convention, Expanded abstracts.